NOVA SCHOOL OF SCIENCE & TECHNOLOGY

DEPARTAMENT OF MATERIALS SCIENCE

BÁRBARA CAEIRO DE AGUIAR E COELHO DO CARMO

BSc in Micro and Nanotechnologies Engineering

THERMALLY CHARGEABLE SUPERCAPACITOR FOR SUSTAINABLE ENERGY HARVESTING OF WASTE HEAT

MASTER IN MICRO AND NANOTECHNOLOGIES ENGINEERING

NOVA University Lisbon

October, 2023

NOVA SCHOOL OF SCIENCE & TECHNOLOGY

DEPARTAMENT OF MATERIALS SCIENCE

THERMALLY CHARGEABLE SUPERCAPACITOR FOR SUSTAINABLE ENERGY HARVESTING OF WASTE HEAT

BÁRBARA CAEIRO DE AGUIAR E COELHO DO CARMO

BSc in Micro e Nanotechnologies Engineering

Adviser: Inês Isabel Fortuna Neves Fernandes da Cunha,
Post-doctoral Researcher, NOVA University Lisbon

Co-advisers: José Tiago Macedo de Carvalho,
MsC, NOVA University Lisbon
Joana Coutinho Sousa,
NOS Inovação S.A.

Examination Committee:

Chair: Rui Alberto Garção Barreira do Nascimento Igreja,
Associate Professor, FCT-NOVA

Rapporteurs: Ana Catarina Bernardino Baptista,
PhD Researcher, FCT-NOVA

Adviser: Inês Isabel Fortuna Neves Fernandes da Cunha,
Post-doctoral Researcher, FCT-NOVA

Members: José Tiago Macedo de Carvalho,
MsC, Another University
Joana Coutinho Sousa,
NOS Inovação S.A.

MASTER IN MICRO AND NANOTECHNOLOGIES ENGINEERING

NOVA University Lisbon
October, 2023

Thermally Chargeable Supercapacitor for Sustainable Energy Harvesting of Waste Heat

This document was created with Microsoft Word text processor and the NOVAthesis Word template [1].

Para o meu irmão.

ACKNOWLEDGMENTS

To begin, I want to express my gratitude to Professor Elvira Fortunato and Professor Rodrigo Martins. They not only paved the way for me and colleagues to delve into the realm of future technologies and actively engage in shaping that future but also granted us access to the resources of CENIMAT|i3N and CEMOP. This access proved instrumental in connecting with the essential equipment crucial for my growth in the realm of micro and nanotechnology engineering and the realization of this project. I extend a heartfelt acknowledgment to all the professors who have played a significant role in shaping my understanding and education in this specialized field.

To my supervisor, Dr. Inês Cunha, I would like to express my deepest gratitude. Her guidance, which provided the concept and basis for the creation of the TCSC, along with all her knowledge in the field of electrolytes, was invaluable for the successful completion of this challenge. Thank you for always pointing out the path I should follow, for your constant support and patience at all times, and above all, for the trust you placed in me. I appreciate you dedicating significant time and effort to help me organize the thesis properly over the last few weeks. Every hour invested was fundamental to the success of this project, and I am sincerely grateful for all your guidance and support.

To Tiago Carvalho, I want to express my deepest gratitude for all the valuable instruction you have provided me in the vast field of energy and supercapacitors. Every lesson shared, every insight conveyed has been a key element in my understanding and progress in this challenging domain. In addition to the knowledge imparted, I want to thank you for the unconditional support I received from you. Throughout this journey, you were always by my side, maintaining calm in challenging moments and showing a tireless willingness to help, regardless of the time of day. I sincerely thank you for having been essential for me to reach this point. The journey was challenging, but your presence and assistance made it a little lighter.

To Professor Luís Pereira, my sincere thanks not only for the comprehensive training provided during the course but also for introducing me to this project. His guidance was invaluable, and I am genuinely grateful for all the contributions he shared throughout my project developments. My gratitude also extends to Joana Sousa and the entire NOS team, whose support pushed me toward the successful culmination of this project.

To Beatriz Coelho, I would like to express my deepest gratitude for her crucial role in the development of the measurement setup and thermal control. Without her, it would not have been possible to prove the concept proposed in this work. I sincerely thank her for her essential contribution.

I cannot imagine reaching this point without the invaluable contributions of Raquel, Bruno, Madalena, and everyone else in the lab. Your ideas and sometimes urgently needed training were fundamental

to the completion and production of my prototype. I am deeply grateful and thankful to each and every one of you.

Quero agradecer à minha família. À minha mãe e ao meu pai, por me terem sempre educado a dar 100% de mim em tudo o que faço e por estarem sempre disponíveis para me ajudar em tudo o que precisava, espero que saibam que quando crescer quero ser como vocês. Ao meu irmão, pelo carinho, por todos os momentos que passámos juntos, por arrumares a mesa de todas as vezes que não conseguia (ah, e continua sempre a chatear-me o juízo, se não for assim não é a mesma coisa). Aos meus avós, por todo o amor incondicional que têm por mim.

À Cataloures, sem ti nada disto teria sido possível. Por me teres apoiado e ouvido sempre que precisava, por tornares estes últimos meses um pouquinho mais alegres, e pelas tuas gargalhadas contagiantes. À Sieira, por todos os almoços, por me compreenderes e acolheres tão bem como fizeste, obrigada madrinha. Ao Mané, ao Pequito, à Maraianaia, ao Ricky e ao Fonsi pelos momentos incríveis que passamos. Ao Gui e ao João, por nunca se terem esquecido da sua amiguinha de nano e por todos os momentos de risada que tivemos. Espero que saibam que sem vocês estes 5 anos nunca teriam sido tão incríveis como foram e o quanto eu gosto de vocês, não poderia ter escolhido melhor companhia para os meus anos de faculdade.

Ao meu amor, Ricardo, quero expressar profunda agradecimento pelo amor, apoio e carinho sem medida. Considero-me uma das pessoas mais sortudas por ter encontrado a minha pessoa em ti. Agradeço por teres caminhado ao meu lado neste percurso e por toda a paciência que demonstraste. És verdadeiramente especial.

“The greater our knowledge increases the more our ignorance unfolds.”
(John F. Kennedy)

ABSTRACT

Set-top boxes (STBs) are often overlooked and packed into small areas, which hinders their operation and heat dissipation, causing overheating and compromising functionality and longevity. To address this issue, we propose to combine energy harvesting and storage technologies in a single system, using thermally chargeable supercapacitors (TCSCs). The TCSCs can convert wasted thermal energy from STBs into electric energy, powering warning devices to keep consumers informed about the STB's thermal status. This is achieved using sustainable materials of natural origin, such as cellulose/paper and cork, and scalable coating/printing technologies for large-scale production at low-cost, while ensuring recyclability.

One of the key materials of the supercapacitors is the electrolyte layer. Here, cellulose-based electrolytes are produced using a low-cost and sustainable aqueous-based dissolution method of cellulose at low temperatures, followed by a regeneration process to obtain hydrogels. A detailed study of the hydrogel preparation parameters is carried out, focused on the effect of the regeneration agent. Cork particles are also incorporated to study its effect on the ionic and thermoelectrical performance of the electrolyte. Incorporation of cork particles promotes a slight increase in the hydrogel ionic conductivity from 1.37 to 3.25 mS cm^{-1}, reaching an ionic Seebeck coefficient of 2.04 mV K^{-1}.

The optimized electrolytes are impregnated on paper substrate to fabricate planar interdigitated SCs with screen-printed carbon electrodes, which play the role of current collector and active material. The SCs based on cellulose:cork electrolyte exhibit a specific capacitance of 3.38 mF cm^{-2}, surpassing those with cellulose-based electrolytes (2.58 mF cm^{-2}). Additionally, both devices also display excellent capacitance retention of 114% and 143% after 10000 cycles, respectively. Six SCs connected in series can power a wristwatch for 4 minutes. Regarding the thermoelectric performance, the fabricated SCs reach a peak thermovoltage of 2.47 mV for a 20 ºC temperature differential, demonstrating the potential of repurposing waste heat generated by STBs as an external power source for future electronics.

Keywords: Cellulose; cork; thermal waste; supercapacitors; energy harvesting; paper electronics; sustainability.

RESUMO

As *Set-top boxes* (STBs) são frequentemente negligenciadas e compactadas em espaços reduzidos, dificultando sua operação e dissipação de calor, o que pode resultar em sobreaquecimento e comprometer a funcionalidade e a longevidade. Para resolver esse problema, propõe-se a integração de tecnologias de recolha e armazenamento de energia num único sistema, utilizando supercondensadores termicamente carregáveis (TCSCs).

Os TCSCs têm a capacidade de converter a energia térmica dissipada pelas STBs em energia elétrica, alimentando dispositivos de alerta para manter os consumidores informados sobre o estado térmico da STB. Para isso, materiais sustentáveis de origem natural, como a celulose/papel e a cortiça, juntamente com tecnologias de revestimento/impressão escaláveis são usadas para produção em grande escala e baixo custo, garantindo simultaneamente a reciclabilidade.

Um componente essencial dos SCs é o eletrólito. Neste caso, eletrólitos à base de celulose são produzidos utilizando um método de dissolução aquosa de baixo custo e sustentável da celulose a baixas temperaturas, seguido por um processo de regeneração para obter hidrogéis. Um estudo detalhado dos parâmetros de preparação do hidrogel é conduzido, focando no efeito do agente de regeneração. Além disso, partículas de cortiça são incorporadas para estudar o seu impacto no desempenho iónico e termoelétrico do eletrólito. A inclusão de partículas de cortiça promove um ligeiro aumento na condutividade iónica do hidrogel, de 1.37 para 3.25 mS cm^{-1}, alcançando um coeficiente de Seebeck iónico de 2.04 mV K^{-1}.

Os eletrólitos otimizados são impregnados no substrato de papel para fabricar SCs planares interdigitais com elétrodos de carbono impressos por serigrafia, que atuam como coletor de corrente e material ativo. Os SCs baseados no eletrólito de celulose:cortiça apresentam uma capacidade específica de 3.38 mF cm^{-2}, superando os SCs com eletrólitos à base de celulose (2.58 mF cm^{-2}). Além disso, ambos os dispositivos demonstram excelente retenção de capacidade, de 114% e 143%, respetivamente, após 10000 ciclos. Seis SCs ligados em série podem alimentar um relógio de pulso por 4 minutos.

Quanto ao desempenho termoelétrico, os SCs fabricados atingem uma tensão termoeléctrica de pico de 2.47 mV para um diferencial de temperatura de 20 ºC, evidenciando o potencial de reaproveitamento do calor residual gerado pelas STBs como fonte de energia externa para a eletrónica do futuro.

Palavras chave: Celulose; cortiça; resíduos térmicos; supercondensadores; recolha de energia; eletrónica de papel; sustentabilidade.

CONTENTS

LIST OF FIGURES

LIST OF TABLES

ACRONYMS

1D	One-dimensional
2D	Two-dimensional
3D	Three-dimensional
CCE	Cellulose:Cork-based Electrolyte
CE	Cellulose-based Electrolyte
CNT	Carbon nanotube
CV	Cyclic Voltammetry
EDL	Electrical double layer
EES	Electrochemical Energy Storage
EG	Ethylene glycol
EIS	Electrochemical Impedance Spectroscopy
ESD	Energy Storage Device
ESR	Equivalent series resistance
GAA	Glacial Acetic Acid
GCD	Galvanostatic Charge/Discharge
GPE	Gel polymer electrolyte
H_3PO_4	Phosphoric acid
IoT	Internet of Things
Li^+	Lithium cations
LIB	Lithium-ion battery
LiOH	Lithium hydroxide

MCC	Microcrystalline cellulose
MWCNT	Multi-walled carbon nanotubes
PET	Polyethylene terephthalate
PVA	Polyvinyl alcohol
R2R	Roll-to-roll
RH	Relative humidity
Rs	Sheet resistance
SC	Supercapacitor
SDG	Sustainable Development Goal
SEM	Scanning electron microscope
S_i	Ionic Seebeck coefficient
SPE	Solid polymer electrolyte
STB	Set-top box
TCSC	Thermally Chargeable Supercapacitor
TGA	Thermogravimetric analysis
UV	Ultraviolet

SYMBOLS

$\boldsymbol{\sigma_i}$	Ionic conductivity
ΔT	Thermal gradient
A	Area
$\mathbf{C_{f=100mHz}}$	Capacitance at a frequency of 100 mHz
Cs	Specific storage capacitance
E	Energy density
^{o}C	Temperature unit
OVW	Operating voltage window
P	Power density
$\mathbf{R_b}$	Bulk Resistance
$\mathbf{S_i}$	Ionic Seebeck coefficient
$\mathbf{V_{OC}}$	Open circuit Voltage

1

INTRODUCTION

1.1 Motivation and objectives

In today's digital era, set-top-boxes (STBs) have become an integral part of households, consisting of electronic devices that connect to a television and signal source, transforming the signal into visible content on the screen.

Efforts have been made towards STBs with aesthetic and seamless designs, and there is a relentless drive to make these devices more compact and efficient, resulting in a higher component density on a smaller printed circuit board area. However, this reduction in board space, which houses all the functional modules of the STB [1], contributes to side effects, particularly increased heat in miniaturized versions of these devices. Furthermore, STBs are commonly installed in overlooked locations and small spaces, also creating substantial operational and thermal challenges. The complexity of this installation hinders effective heat dissipation, leading to overheating problems that impact the functionality and longevity of the equipment.

A dedicated study on STBs [2] compared two distinct models of boxes (box UMA V.1 vs. box UMA V.2 – miniaturized version of UMA V.1, Figure 1.1) revealing that box UMA V.2 can reach temperatures between 38 and 47 ºC, depending on the mode-operation, approximately 7 ºC higher than the previous non-miniaturized version.

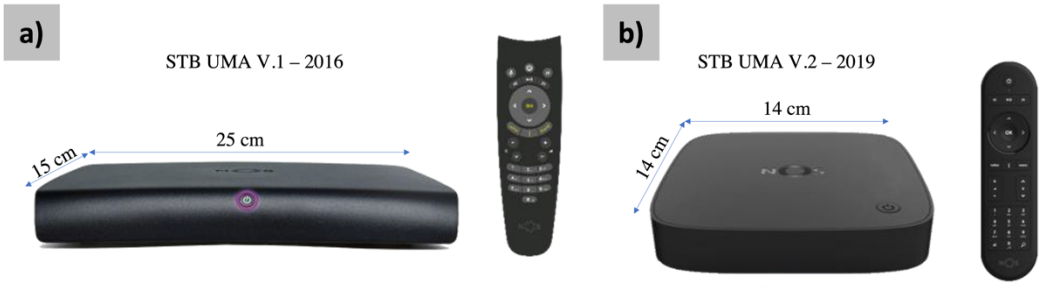

Figure 1.1 – Size comparison of the two STB UMA versions: a) STB UMA V.1 (2016) and b) STB UMA V.2 (2019).

The "overheat-challenge" of the STBs can be seen as an opportunity in the perspective of thermal waste as a source of energy to be harvested and used to store electrical energy that can be repurposed to power additional devices. Recognizing the importance of reusing the thermal energy wasted by the STBs is crucial to promote sustainable behavior, aligning with the Sustainable Development Goals (SDGs) [3].

With these considerations in mind, ensuring proper thermal control of the device throughout its lifetime is imperative—a concern shared by both service providers and building occupants. To address this issue, we propose combining energy harvesting and storage technologies into a single system using thermally chargeable supercapacitors (TCSCs), capable to convert the thermal energy discarded by STBs into usable energy. The harvested-stored energy could potentially be used to power an alarm system, which can be a wireless communication system (e.g. Bluetooth), colorimetric sensor, or a sound alert, which informs building occupants about the STB's thermal condition. TCSC production is based on low-cost, sustainable printing techniques, using paper as the substrate. This approach, suitable for Roll-to-roll (R2R), makes the process environmentally friendly, flexible, and economically viable.

Our study aims for a comprehensive analysis, focusing on i) the electrolyte layer formulation and characterization, ii) electrodes design, iii) electrolytes and electrodes integration in SCs on paper substrates using printing/ coating technologies, iv) overall SCs performance assessment, and v) proof-of-concept of TCSCs.

Concerning the electrolyte layer, cellulose-based electrolytes (CE) were produced using a low-cost and sustainable aqueous dissolution method of cellulose at low temperatures, followed by a regeneration process to obtain hydrogels.

Taking advantage of the natural porous morphology of cork and its contribution to thermal insulation, we also explore the impact of adding cork particles to the CE formulation to tailor the thermal properties of the electrolyte with the aim of keeping the thermal gradient through longer periods without compromising the electrochemical properties. Detailed studies on finding balanced thermal/ionic conductivity properties will ultimately contribute to better performances of the TCSCs.

1.2 State-of-the-art

The approach proposed in this thesis focuses on electrolytes' development and their integration in SCs, with emphasis on a particular class of SCs that are charged by thermal gradient, the TCSCs. From a sustainability perspective, low-cost and environmentally friendly materials and technologies have been incorporated, placing emphasis on the utilization of paper technology as a support to host devices. Additionally, cellulosic and cork materials were employed to formulate the electrolyte, while coating/ printing technologies were used to fabricate the SCs/TCSCs. This approach not only exploits the potential of thermal waste as an energy source but also integrates sustainable and reusable practices into all stages of SCs and TCSCs development.

1.2.1 Energy storage devices: supercapacitors

The increasing demand for energy storage devices (ESDs) is fueled by the necessity to meet the intricate energy requirements of contemporary society, with the energy from ESD emerging as a promising solution to power sensors in the Internet of Things (IoT) and addressing the growing needs for energy storage. Electrochemical energy storage (EES) technologies, including supercapacitors (SCs) and lithium-ion batteries (LIBs), have consequently garnered significant interest in response to these evolving energy challenges [4]–[6].

SCs take the spotlight in EES systems, offering notable advantages such as high efficiency, an extended life cycle, and the use of sustainable materials, resulting in minimal maintenance costs [7]–[10]. SCs exhibit a rapid discharge time of 1-10 seconds, outshining LIBs with their discharge time of 10-60 minutes. Both SCs and LIBs showcase impressive cyclic stability, with SCs exceeding 30,000 hours and LIBs surpassing 500 hours [4]. These exceptional qualities position supercapacitors as a key focus in research for efficient energy supply and storage [10]–[12].

SCs are ESDs based on electrochemical processes [6], [13], consisting of two electrodes separated by an ion-conducting electrolyte [6], [9], [13], [14]. The electrodes are usually made of porous materials (such as activated carbon, graphene, or metal oxide), which provide a high surface area for adsorption of ions from the electrolyte [13], [14]. When a voltage is applied between the electrodes, ions in the electrolyte are attracted to the electrode surfaces, forming a layer of electrical charge known as an electrical double layer (EDL). The EDL, although extremely thin with dimensions on the order of Angstroms, is responsible for the capacitance of the SC [6], [9], [10], [13], [14]. Despite its thinness, the EDL's large surface area results in a high specific capacitance [8]. These devices store electrical energy in an electric field between the electrodes, unlike conventional batteries which store chemical energy [13], [14].

SCs can be characterized in three types according to the employed active materials and involved charge storage mechanisms: (i) the electrical double layer capacitor (EDLC) where charges are electrostatically reversible stored at the electrode/electrolyte interface; (ii) pseudocapacitors where charges are stored owing to fast and reversible redox reactions, and (iii) hybrid capacitors in which the charge storage mechanism of the two electrodes is not similar and the storage principle is based on both Faradaic and non-Faradaic. Figure 1.2 illustrates the different types of SCs and the electrode materials that compose them.

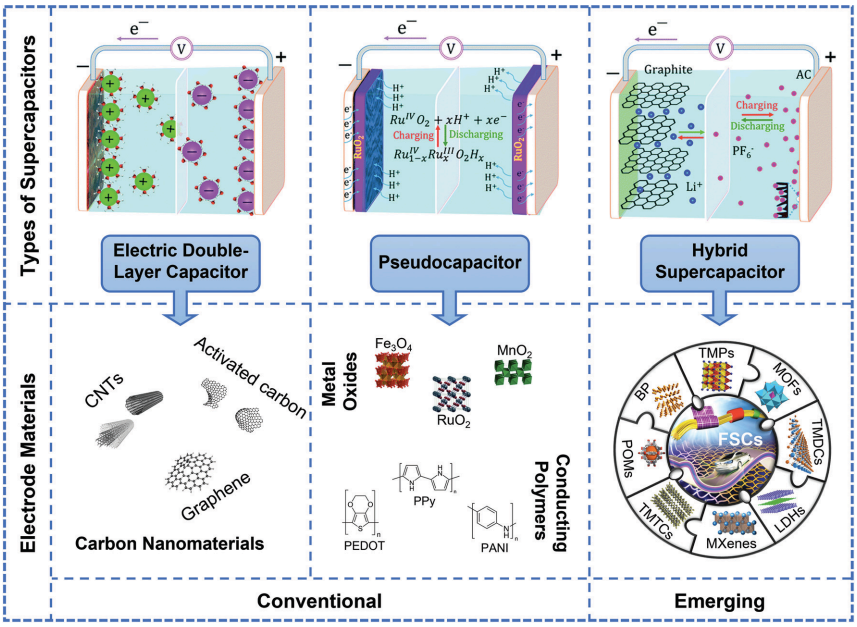

Figure 1.2 – Different types of SCs and the electrodes materials that compose them [6].

In terms of materials, the growing demand for flexible electronics has spurred advancements in SC technology. These SCs feature electrodes made on flexible substrates, carbon paper/fabric, carbon-based hydrogels, polyethylene terephthalate (PET), Kapton, cellulose paper, and textiles, are employed as substrates. SCs are typically composed of carbon-based electrode materials, such as activated carbon, ordered mesoporous carbon, carbon black, graphene, carbon nanotubes (CNTs) and carbon aerogels because of their high electrical. Table 5.1 lists current state-of-the-art in SCs, detailing materials, configuration and performance achieved.

Traditional SCS are based on liquid electrolytes, which posed significant risks in terms of leakage and safety. The new emerging SCs, with the various configurations displayed in Figure 1.3, have been designed to be safer, perhaps even flexible, widening their potential applications. Therefore, new electrolytes have also been developed to allow flexibility, conformability, reparability and at the same time, ensure safety. Gel polymer electrolytes (GPEs) have been mentioned in the literature as a promising approach since their properties fall between the liquid electrolytes and the solid polymer electrolytes (SPEs). The former exhibited high ionic conductivity (10^{-3}–10^{-2} S cm^{-1}) but lack in safety, whereas the latter display low ionic conductivities (10^{-8}–10^{-5} S cm^{-1}) and poor interface between the electrode materials. Nevertheless, it is a safer option and can also work as separator.

In GPEs, the polymer acts as a matrix and the ions move in the solvent. When water is used as the solvent in GPEs, they are also referred as hydrogel-based polymer electrolytes. Nevertheless, the high amount of water present makes difficult to extend the operation voltage window since the decomposition voltage of water is at 1.23 V, in contrast with GPEs that used organic solvents.

Regarding the electrode configuration (Figure 1.3), SCs can be categorized into one-dimensional (1D) fiber-type architectures (e.g., parallel, twisted, and coaxial), two-dimensional (2D) flat architectures (e.g., sandwiched thin-film electrodes, interdigitated finger-type, and an array of micro-supercapacitors), and three-dimensional (3D) architectures (e.g., kirigami/origami, sponge, and textile structures). This design flexibility significantly expands its potential applications in various portable and flexible electronic devices [6].

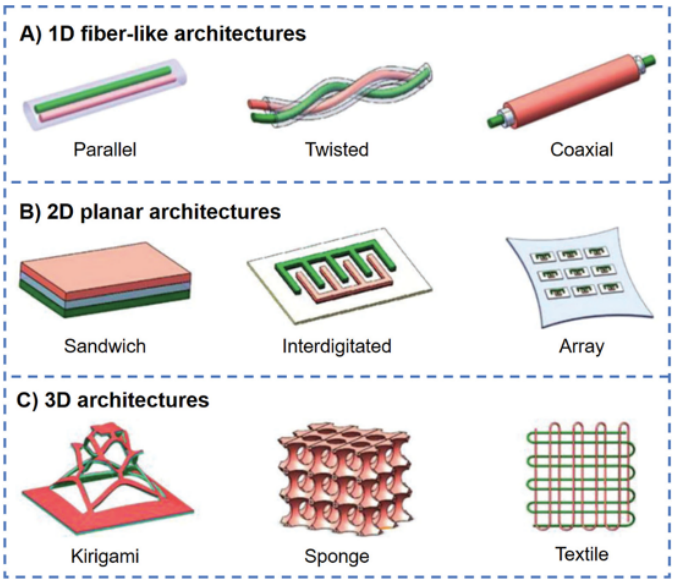

Figure 1.3 – Schematic representation of three main typical architectures of SCs: A) 1D fiber-like architectures; B) 2D planar architectures; and C) 3D architectures. The orange and green colors represent individual electrodes while the grey color represents the electrolyte [6].

Table 5.1 shows promising 2D SCs reported in the literature, materials used and their electrochemical performance. The development of more advanced all-in-one smart technologies integrating both energy harvesting and storage functionalities is a promising breakthrough to ensure a sustainable and endurable energy supply. This endeavor represents a major leap in the field of IoT technologies to address the key requirements of self-powered miniaturized electronics.

1.2.1.1 Thermally chargeable supercapacitors

TCSCs are a particular class of SCs that are able to store electrical energy harvested from a thermal gradient established between the electrodes of the device. Therefore, the TCSCs combines two distinct mechanisms: i) the conversion of thermal energy into electrical energy within a temperature gradient and ii) the storage of energy in a supercapacitive manner.

Regarding the conversion of thermal energy into electrical energy, TCSCs utilize an energy harvesting mechanism based on the Soret effect [6], [9], [13], [15], [16], which involves the diffusion of ionic charge carriers (cations and anions) in an electrolyte, moving towards the surface of conductive electrodes driven by a temperature gradient, as illustrated in

Figure 1.**4** [6], [7], [9].

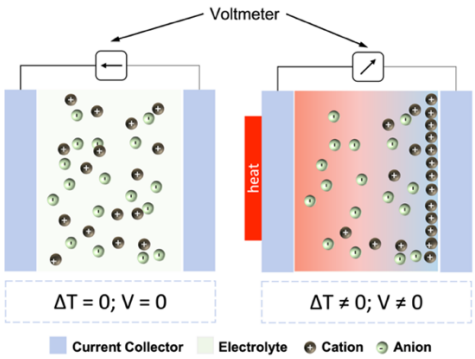

Figure 1.4 – Schematic of thermoelectric conversion and storage based on the Soret effect in an TCSC. (adapted from [15]).

The unique synergy between energy storage and the ability to harvest energy from temperature gradients makes TCSCs a very promising technology. These devices represent autonomous multitasking units, integrating two distinct functions into a single unit. [6], [17]. This technology is emerging as a remarkable solution for harnessing waste heat released by sources of low thermal quality (<250 ºC), including industrial processes, vehicle engines, domestic use, transportation, and human metabolism. Its applications extend to powering low-consumption electronic devices, particularly in scenarios that demand energy efficiency, storage in variable thermal conditions, and efficient conversion of waste heat into electricity [6]. Table 5.2 displays the most recent TCSCs reported in the literature. A notable example is the work of Pires et al. [18], who introduced an all-in-one planar TCSC produced through a photolithography process. This device combines carbon nanotubes as the electrode material with polyvinyl alcohol (PVA) doped with phosphoric acid (H_3PO_4) as a solid-gel polyelectrolyte.

The ionic thermoelectric effect acts as an internal electrical generator that can charge the EDLC of the SC [18]–[20]. In brief, the concept of an TCSC is carried out in four phases out in four stages: 1) initial state; 2) charge; 3) storage; and 4) discharge state, as illustrated in the Figure 1.5.

At the beginning of the first phase, the ions in the electrolyte are randomly distributed, corresponding to the initial state of thermal charging behavior. With the application of a certain ΔT between the two electrodes, the ions will gradually accumulate in the cold electrode, due to the Soret effect, generating an increasing thermal voltage. In the second phase, a closed circuit is built with an external resistance, keeping thermal gradient (ΔT) constant. The introduction of an external resistance will allow the electrons to move from one electrode to the other, causing the number of accumulated ions to reach maximum concentration and the voltage to decrease until it is balanced at ≈0 V, corresponding to the charged state. In the third phase, the ΔT is removed, and the external circuit is switched off, and the energy storage process takes place. As the circuit is open, the accumulated ions again diffuse and distribute themselves evenly across the electrodes. In the fourth phase, the external circuit is reconnected, and an imbalance of the electrolyte ions begins to appear, corresponding to the discharged state.

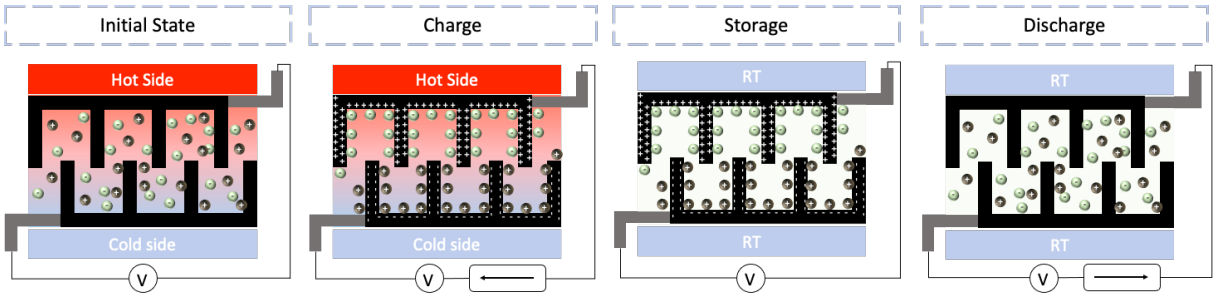

Figure 1.5 – Schematic explanation of the electrochemical operation mechanism of the ITSC highlighting the electrolyte ion motion during the thermal charging, where 1) is the initial stage, 2) is the charged state, 3) is the storage state, and 4) is the discharged state; the "-" symbol corresponds to the electrolyte anions and the "+" symbol to the electrolyte cations. (based on reference [6])

1.2.2 Printing techniques on paper substrates: screen-printing

Printed electronics is an emerging technology that consisting of simple, fast, cost-effective, and high-volume R2R manufacturing processes that enable the fabrication of electronic devices on flexible substrates at low-cost. This innovation opens new possibilities for applications in portable electronics, not only due to the potential for manufacturing ultra-efficient devices but also because it aligns with the

ecological demands of modern society. It plays a crucial role in the evolution of electronic devices, effectively responding to contemporary standards and needs [21]–[24].

Flexible, ubiquitous paper substrates emerge as the most suitable option for creating an affordable and scalable printed electronics production, due to its hydrophilicity, porosity, availability, and flexibility [2], [24]. It is biodegradable and recyclable, making it a more economical and sustainable choice compared to plastic substrates. Several studies demonstrate its effectiveness as a support for numerous applications, such as transistors [21], [22], supercapacitors [25], solar cells [26] , sensors [27], among others, highlighting the compatibility between paper and printing technologies.

From a vast list of printing techniques, screen printing stands out due to its simplicity and compatibility with various substrates. Figure 1.6 illustrates the screen-printing process and respective accessories, including a substrate, a screen-mesh (usually made of polyester or metal threads), a squeegee (plastic or rubber sheet) and ink [28] . The inks used must have a high viscosity (0.03 – 50 Pa s) and exhibit thixotropic (shear-thinning) behavior to avoid simply running through the screen-mesh [28]–[30].

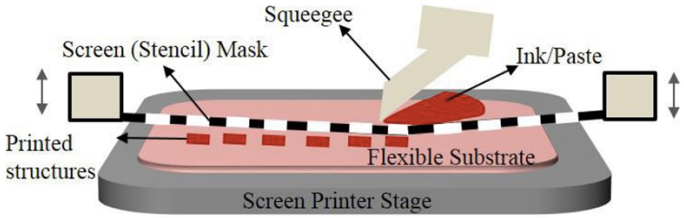

Figure 1.6 – Schematic of screen-printing technique. [29]

The screen printing procedure involves positioning the substrate under the standardized screen-mesh and pushing the ink through it with the help of the squeegee. As a result, the pattern is transferred only to the permeable areas of the screen-mesh. The pattern on the mesh is selectively defined usuin a photo-polymerized emulsion. This creates the non-printing areas , leaving the non-polymerized areas available for the ink to pass through [29].

The resolution and thickness of the print are influenced by the density of the mesh and the properties of the ink and substrate[23], [30]. A mesh with smaller pores significantly increases resolution, providing greater detail in the pattern [23]. Additionally, parameters such as pressure, angle, and speed of the squeegee in relation to the mask, as well as the space between the mask and the substrate, among other factors, during the printing process also affect the quality of the resolution [5], [28].

Widely adopted in various areas due to its advantages, screen printing is particularly preferred in paper electronics. Its advantages include the ability to print on flexible substrates, allowing the efficient integration of electronic components on curved or flexible surfaces. In addition, screen printing offers high precision and resolution, contributing to the production of paper electronic devices with fine detail. The versatility of materials and the ability to print in large volumes efficiently also highlight screen printing as an advantageous choice in paper electronics [28], [29] Xu et al. demonstrated the successful printing of Fe_2O_3 $^{-5}$ wt% CNT composite material to fabricate a SC, employing screen-printing as the chosen method for producing the electrodes of their SC [24].

1.2.3 Sustainable natural materials

1.2.3.1 Cellulose and its derivatives

Cellulose, a highly abundant and widely available biopolymer in nature, surpasses 7.5×10^{10} tons in annual production. Widely recognized for its renewability, biocompatibility, cost-effectiveness, non-toxicity, and biodegradability, cellulose boasts diverse applications [28], [31]–[35]. Its extraction from renewable resources underscores its significance, particularly in paper production, textiles, and construction materials, where its unique properties contribute to both environmental sustainability and versatile manufacturing processes [31], [35].

Composed of D-anhydroglucopyranose units, cellulose forms linear polymer chains, a primary structural component of cell walls in various organisms. This hierarchical structure imparts cellulose with linearity and functionality [28], [31], [34]–[36]. Processing native cellulose is challenging due to its long, rigid chain and robust hydrogen bonds, leading to various industrial derivatives, such as rayon, cellulose ether, nitrocellulose, cellulose acetate, carboxymethyl cellulose, ethyl cellulose, microcrystalline cellulose (MCC), and regenerated fibers [31], [35].

Multicomponent solvent systems have been created to produce new regenerated cellulose materials through dissolution, molding and regeneration processes. However, traditional solvents, such as lithium chloride/N,N-dimethylacetamide, have limitations due to volatility, toxicity and cost, restricting their application to laboratory scales. As a successful alternative, a simple and fast route was developed using more accessible and less toxic solvents to dissolve cotton linter at low temperatures. This resulted in cellulose hydrogels without hazardous by-products. An example is the use of the lithium hydroxide (LiOH)/urea system, where the dissolution mechanism involves the formation of inclusion complexes, facilitating the rapid dissolution of MCC, resulting in transparent solutions. The addition of acid solutions, alcohols, acetone, or the application of high temperatures breaks down the cellulose inclusion complex, leading to the rapid formation of physically regenerated cellulose hydrogels [28].

1.2.3.2 Cork

Cork, derived from the bark of the cork oak tree in Portugal (*Quercus suber L.*), stands out as a natural, biodegradable, renewable, and sustainable biocomposite. In addition to being 100% reusable and recyclable, it is harvested every 9 years, preserving the trees. With its carbon dioxide capture properties and a crucial role against climate change, cork is essential for sustainability, emerging as a vital economic sector in Portugal [28], [37], [38].

Cork possesses a unique composition dominated by suberin, an aliphatic-aromatic polyester, constituting 30-50% of the cell wall. This porous honeycomb structure comprises closed, pentagonal or hexagonal, hollow, thin-walled cells containing approximately 80% of an air-like gas. Additional chemical elements, such as lignin (15-30%), polysaccharides like cellulose and hemicelluloses (6-25%), and extractives (8-20%), are also notable in its composition [28]. Its structural complexity imparts unique and desirable properties to cork, serving as an excellent thermal and acoustic insulator, making it waterproof, fire-resistant, wear-resistant, and incredibly light.

The cork industry faces the challenge of managing large volumes of waste, especially in cork stopper production, representing 20-30% of annual production in Portugal, which is primarily utilized as fuel for energy generation [28], [37], [38].

2

MATERIALS & METHODS

This section aims to present all the steps there were taken to prepare and characterize the cellulose and cellulose/cork electrolytes, as well as the design and fabrication process of the TCSCs on paper.

2.1 Cellulose-based electrolytes

2.1.1 Preparation of cellulose electrolytes

Inspired in the procedures reported in the literature for the dissolution of cellulose [28], [39], different strategies were employed to prepare cellulose-based electrolytes (CE).

Cellulose dissolution medium was formulated by combining 4.6 wt.% LiOH (0.46 g, Sigma-Aldrich ≥98 %), 15 wt%. urea (1.5 g, Carl Roth, ≥99.5 %) with 80.4 wt%. deionized water (8.04 g, Millipore). After obtaining a homogeneous and transparent solution, the solvent mixture was cooled in a freezer at -25 ºC until solidified.

The solution was left to thaw at room temperature, and 5 wt.% of microcrystalline cellulose (MCC, 0.5 g in 10 g of solution, Sigma-Aldrich, powder: 20 μm) was slowly added to the solvent system (9.5 g) while stirring vigorously at -8 ºC until it dissolved completely (≈30 min). To improve cellulose dissolution, a freezing-thawing cycle was carried out.

As schematized in Figure 2.1, 3 mL of the cellulose solution was poured in polystyrene Petri dishes with 55 mm diameter, previously exposed to a ultraviolet (UV) treatment (Novascan PSD-UV with Ozone Elimination System) for 15 min to reduce its hydrophobic effect and improve the spreading of the solution over the entire area.

The regeneration process was performed using glacial acetic acid (GAA, Sigma-Aldrich, ≥99) or mixtures of GAA with glycerol (GC, BioXtra, ≥99) or ethylene glycol (EG, Carlo Erba Reagents) with a weight ratio of 1:1. The regeneration process was performed using a Whatman paper (FILTER-LAB), with the same diameter of the petri dishes, soaked in the regeneration solution. The soaked filter paper was then placed on top of the cellulose solution. Table 2.1 describes all the CEs developed.

Table 2.1 – List of CE samples prepared.

Nomenclature	Regeneration solution	Regeneration solution [RS, wt.%]
CM0	GAA	100
GCM	GAA:GC	50:50
ECM	GAA:EG	50:50

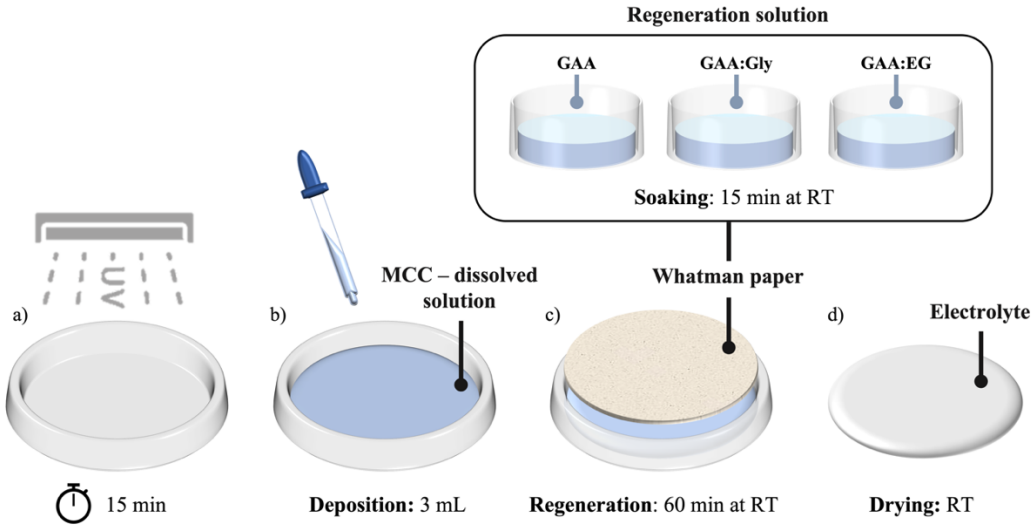

Figure 2.1 – Schematic representation of the electrolyte fabrication process. a) UV-treatment of the petri dish; b) Solvent-casting of the dissolved cellulose solution (3 mL); c) Regeneration process; d) drying of the hydrogel electrolyte at ambient conditions.

2.1.2 Preparation of cellulose:cork electrolytes

Following a previous work on dissolution of cork in aqueous-alkali medium [28] cork particles were obtained from natural cork stoppers of various wine brands were used to obtain cork particles with different granulometries, ranging from <200 µm and 500-800 µm. The cork stoppers were grounded using a domestic grinding machine and sieved to obtain the particles of different sizes. Cellulose:cork-based electrolytes (CCE) were prepared by adding cork particles to cellulose-based solutions using two strategies, following the same procedure described in the previous section.

- **Method 1:** Cork particles were added to the MCC-dissolved solution at various weight ratios (1:99 and 5:95 wt.%) and partially dissolved for different time periods (5-60 minutes).
- **Method 2**: Different amounts of cork particles (0.05 and 0.1 g) were randomly poured in the UV-pre-treated petri-dish, and the 3 mL of the MCC-dissolved solution was poured over the cork particles/ container.

Both methods were followed by the regeneration process using GAA:EG mixture.
A summary of all the developed electrolyte membranes are displayed in Table 2.2 and Table 2.3.

Table 2.2 – List of CCE samples prepared using method 1.

Nomenclature	Cork [C, wt.%] in the MCC-dissolved solution	Cork particles size [µm]	MCC [M, wt.%] in the LiOH:urea aqueous solvent system	Dissolution time [T, min]
M1C2T5	1	< 200	5	5
M1C2T15				15
M1C2T30				30
M1C2T60				60
M5C2T5	5			5
M5C2T15				15
M5C2T30				30

M5C2T60				60
M1C5T5	1	500-800	5	5
M1C5T15				15
M1C5T30				30
M1C5T60				60
M5C5T5	5			5
M5C5T15				15
M5C5T30				30
M5C5T60				60

Table 2.3 – List of CCE samples prepared using method 2.

Nomenclature	MCC [M, wt.%] in the LiOH:urea aqueous solvent system	Cork particles size [µm]	Cork weight [C, g] for 3 mL of MCC-dissolved solution
C2M100	5	< 200	0.1
C2M50			0.05
C5M100		500-800	0.1
C5M50			0.05

2.1.3 Characterization of the electrolytes

The electrochemical characterization of the CE and CCE was carried out at room temperature (23 ± 2°C, ~40% RT) utilizing a Gamry Instruments Reference 600 potentiostat. The electrolytes membranes were placed between two gold electrodes with an active area of 1.77 cm^2 using a typical capacitor configuration, as represented in Figure 2.2(a). Electrochemical impedance spectroscopy (EIS) was performed with an AC voltage of 10 mV, covering a frequency range from 0.1 to 10^6 Hz.

EIS analysis was performed to determine the ionic conductivity (σ_i) of the electrolytes. The ionic conductivity can be determined by the following expression [28]:

$$\sigma_i = \frac{l}{R_b \times A} \quad (1)$$

where R_b is the bulk resistance; l is the thickness of the electrolyte membrane, and A is the surface area.

Thermogravimetric analysis (TGA) was performed to assess the thermal properties of the electrolytes using a STA 449 F3 Jupiter. CE and CCE electrolytes were subjected to TGA analysis in the temperature range of 20.5 to 550 ºC at a heating rate of 5 K min^{-1} under nitrogen.

The thermoelectric properties of the electrolytes were investigated using the same capacitor configuration as in EIS measurements. The electrolyte was placed in direct contact between two flat gold electrodes. To monitor the temperature difference between the two electrodes, a thermal analysis camera (testo 872s) and PYROSOFT VIEWER software were employed, as represented in Figure 2.2(b). A temperature difference was induced using a hotplate, and the corresponding Seebeck– induced open voltage was obtained by measuring the open circuit potential on the Gamry Instruments Reference 600 potentiostat. The thermovoltage induced by different ΔT was investigated in the temperature range between 25°C and 45°C.

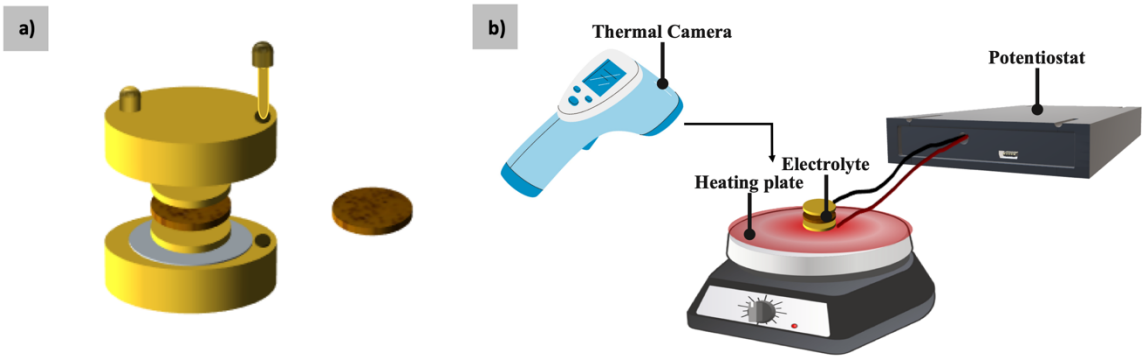

Figure 2.2 – a) Schematic of typical capacitor configuration used for the electrochemical analysis. b) Schematic of the setup used for the thermoelectric analysis of the electrolyte samples.

2.2 Fabrication of the supercapacitor on paper

2.2.1 Impregnation of the electrolyte on paper

As shown in Figure 2.3, a square-shape wax barrier (1 cm wide) was established to enclose the electrolyte within a 1 cm^2 on a 120 g/m^2 office paper substrate (The Navigator Company^{TM}). The wax was inkjet-printed using a Xerox ColorQube printer, and then impregnated into the paper by heating at 120 ºC for 5 minutes. Subsequently, a 30-minute UV-treatment was carried out to promote better spreading of the electrolyte solution, and 100 µL of MCC-dissolved solution was deposited by drop-casting into the well. Before starting the regeneration process, the solution was left to settle on the paper surface for 30 minutes to ensure better paper/electrolyte interface. The regeneration process was conducted for 1 hour, following two strategies: i) drop casting 20 µL of the regeneration solvent (GAA:EG mixture) directly on the electrolyte, or ii) coating the MCC-dissolved solution with a soaked filter paper with the regeneration solvent.

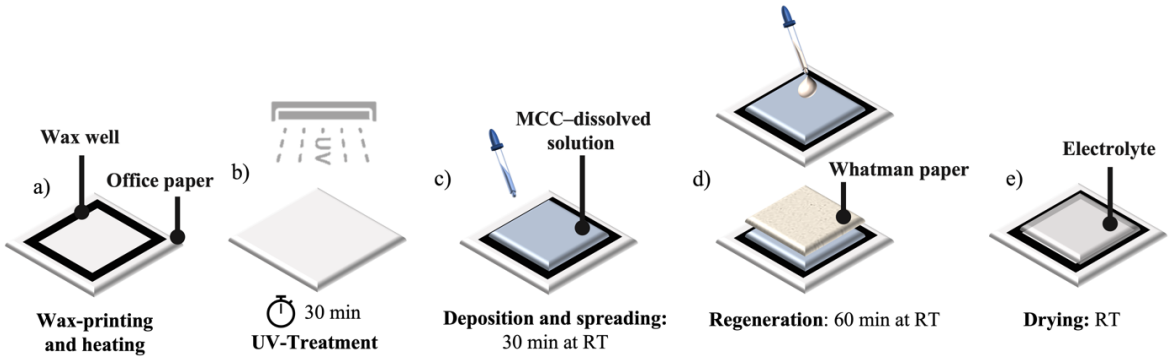

Figure 2.3 – Schematic representation of the electrolyte impregnation on the paper substrate. a) wax-printing and heating; b) UV-treatment of paper; b) Drop-casting 100 µL of the dissolved cellulose; c) Regeneration process: soaking or drop casting; d) Drying at ambient conditions.

2.2.2 Screen-printing of the electrodes on paper

A 30-minute UV treatment was performed on the paper sheet with the electrolyte impregnated to promote better coating of the following active layers of the SC.

Interdigital planar electrodes (with dimensions of 4.62 x 1.27 µm) were screen-printed using a water-based carbon conductive ink (WBC01S, Nanopaint) and a polyester screen with the following characteristics: model 77-55, 190 meshes per inch, 81 µm mesh opening, 55 µm wire diameter, 30% open area and a screen thickness in the range 88-97 µm. The interdigital electrodes were printed directly on top of the electrolyte and then annealed for 1 hour at 50 ºC (configuration 1: paper/electrolyte/electrode).

A different approach was used to fabricate the SCs, starting with the screen-printing on the opposite side of the paper with inkjet-printed wax barriers (without electrolyte), followed by annealing for 5 minutes at 100ºC. The electrolyte was impregnated within the wax barriers following the same procedure detailed in section 2.2.1, as shows in the Figure 3.7 (configuration 2: electrode/paper/electrolyte).

The sheet resistances were measured using the Biorad/Nanometrics Hall Effect system (HL5500PC).

Table 2.4 – Summary of the developed/optimized SCs models.

Nomenclature	Configuration	Electrolyte
TE	**1:** paper/electrolyte/electrode	ECM
BE	**2:** electrode/paper/electrolyte	
BEC		M1C5T30

2.3 Electrochemical analysis of the supercapacitors

The electrochemical performance of the SCs was assessed through a series of electrochemical tests, namely, EIS, cyclic voltammetry (CV), and galvanostatic charge/discharge (GCD) experiments – conducted under temperature-controlled humidity conditions (23 ± 2°C, ~80% RH). These tests were carried out in a two-electrode configuration utilizing a Gamry Instruments Reference 600 potentiostat.

EIS measurements were performed using an AC voltage amplitude of 10 mV covering a frequency spectrum from 0.01 to 10^6 Hz.

CV measurements were performed by sweeping the voltage between 0 and 0.8 V, using different sweep rates (5, 10, 20, 50, 70, 100. 200, and 500 mV s^{-1}). Five consecutive cycles were acquired before subsequent analysis. CV analysis was performed to determine the specific storage capacitance of the device. The specific capacitance can be determined by the following expression [18]:

$$C_s = \frac{1}{2 \times X_t \times v \times \Delta V} \int_{-V}^{+V} i(v) dV \quad (2)$$

where X_t is the active surface area of the device; ν is the potential scan rate, ΔV is the potential window, and *i* is the current intensity.

The GCD characterization of the device is conducted to determine the operating voltage of the supercapacitors. In this analysis, the characteristic capacitive behavior of the device was evaluated by performing consecutive charge and discharge tests at different current densities (5, 10, 20, 50, 70, 100, 150, 200, 250, and 300 µA cm^{-1}). Capacitance retention tests of 10000 CV cycles were also carried out in a scan rate of 200 mV s^{-1}.

The energy density (E) and power density (P) values of the devices, which are considered the key parameters to define the energy storage performance, were determined by considering the operating

voltage, the specific capacitance, and the dimensions of the device. For EDLCs, the E and the P can be calculated from Equation 3 and 4, respectively [18]:

$$E = \frac{1}{2\times3600} \times C_s \times \Delta V^2 \quad (3)$$

and

$$P = \frac{E\times3600}{\Delta t} \quad (4)$$

where E is expressed in W h cm^{-2}, and P is expressed in W cm^{-2}.

Mechanical deformation tests were also conducted on the SCs using a home-made automatic set-up, and 1000 bending cycles were performed, and then were subjected to CV measurements to evaluate the degradation of the devices.

To showcase the scalability of our process, we connected six SCs in series following configuration 2, three-layered carbon electrodes were screen-printed on paper with planar interdigitated design These SCs were printed onto the paper substrate, mirroring the conventional SC process, arranged side by side. Employing NanoPaint's SInk01NP silver ink, we seamlessly connected the six SCs, establishing the necessary interconnections. Subsequently, we meticulously impregnated the electrolyte onto the front of the paper. This methodology not only exemplifies the scalability and effectiveness of our process for larger-scale production but also ensures an interconnected configuration of integrated supercapacitors.

2.3.1 Proof-of-concept: thermally chargeable supercapacitors

To evaluate the thermoelectric potential, a custom-made setup was built to selectively control the temperature of each electrode of the SC, keeping one electrode "hot" and the other "cold", thus inducing a thermal gradient, while recording overtime the thermoelectrical potential obtained. To this end, the respective electrodes of the TCSC were placed on top of two peltiers, as illustrated in Figure 2.4. One peltier is coupled with a Pt100 temperature sensor, connect to a breakout module (MAX31865) which transfer the readings to the arduíno program. The thermal gradient between the two peltiers was induced by a voltage supply.

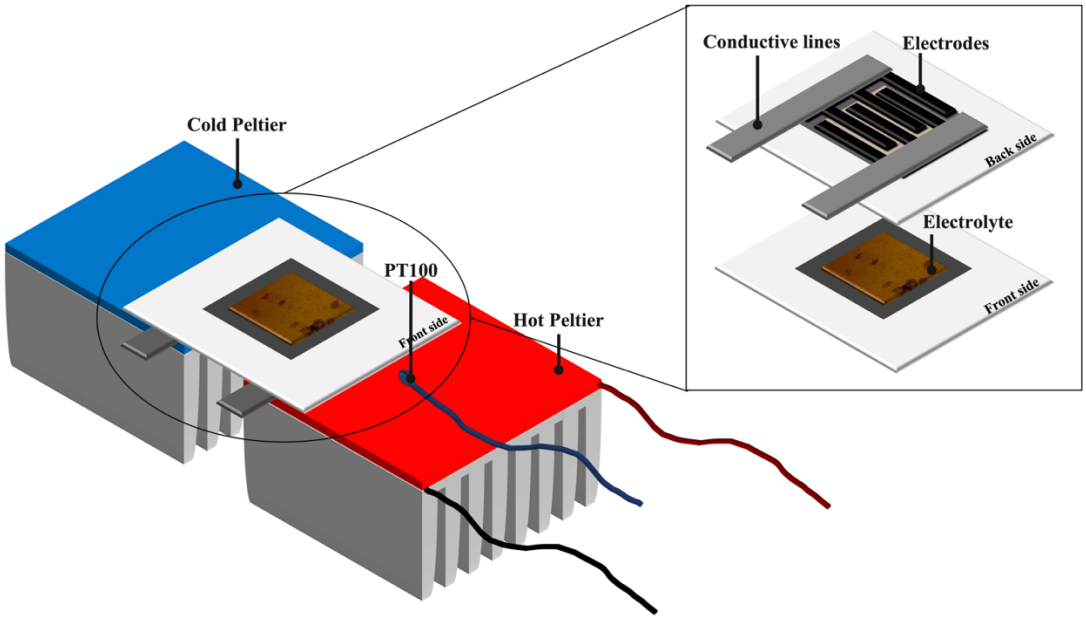

Figure 2.4 – Schematic representation of the custom-made setup to induce the thermal gradient on the SC. The inset characterized the TCSC with CCE electrolyte.

3

RESULTS & DISCUSSION

This chapter aims to present all results achieved during this thesis work. Section 3.1 focuses on the formulation, preparation, and characterization of the developed cellulose electrolytes. Section 3.2 explores the procedures involved in producing the SCs: impregnation of the electrolytes in paper and printing the electrodes using screen printing. Additionally, we provide detailed insights into all the electrochemical analyses conducted, encompassing a variety of electrochemical tests, such as EIS, CV, GCD, capacitance retention, as well as flexibility tests. Finally, a proof-of-concept of SCs charged by energy thermal waste is demonstrated.

3.1 Formulation of electrolytes

3.1.1 Cellulose-based electrolytes

CEs were produced using a simple, fast, low-cost, and environmentally friendly method that involves dissolving MCC at low temperature in an aqueous alkaline hydroxide/urea solvent system.

As shown in Figure 3.1a), a completely transparent and slightly viscous solution is obtained due to the good solubility of the cellulose in the pre-cooled aqueous LiOH/urea solution. This result is achieved through a freeze-thaw process that facilitates the rapid dissolution of cellulose in a few minutes (~5 min), under vigorous stirring at low temperatures (below -8 ºC). The transparency of the solutions is linked to the effectiveness of the cellulose dissolution process.

The dissolution of cellulose in the presence of an alkaline ionic salt (LiOH) results in the release of lithium cations (Li^+) that play the role of charge carriers in the electrolyte medium, contributing to the ionic conductivity when subjected to an electric field. However, the presence of OH^- imparts a highly alkaline nature to the solution (pH = 14), rendering it unsuitable for direct application in devices without causing damage to the deposited layers.

To convert the MCC-dissolved solution into a hydrogel, 3 mL of solution was poured in a petri dish, followed by a regeneration step. Filter papers with the same shape and size of the petri dish were soaked in the prepared regeneration solutions (GAA, GAA:GCs, and GAA:EG), and then positioned with a tweezer on top of the solubilized cellulose for 1 hour, slowing converting into a hydrogel.

Figure 3.1b) illustrates the resulting hydrogel membranes after cellulose regeneration, which exhibit flexibility and transparency.

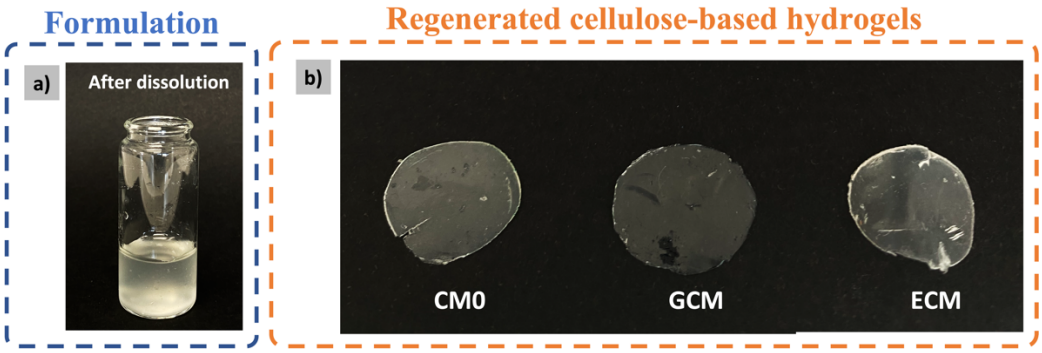

Figure 3.1 – Photography of the a) MCC-dissolved solution and b) regenerated cellulose-based hydrogels obtained using different regeneration solutions.

3.1.2 Cellulose:cork-based electrolytes

Cork, with its unique composition and porous hierarchical structure, stands out for its diverse properties, such as effective thermal, electrical, and acoustic insulation, low density, impermeability to liquids and gases, resistance to fire, high temperatures, as well as exceptional friction resistance, elasticity, compressibility and remarkable chemical resistance [28]. Therefore, cork particles were incorporated into the cellulose electrolyte in order to study their influence on the electrolyte's ionic and thermoelectric performance.

Figure 3.2 shows the solutions resulting from methods 1 and 2, and respective membranes (Figure 3.2c and d). In method 1, cork particles are incorporated into the solubilized cellulose solution at different weight ratios and partially dissolved. It can be observed that the solution takes on a darker brown color for longer periods of dissolution and higher amounts of cork (Figure 3.2b). A similar observation occurs when using method 2, where cork particles are evenly spread on the petri dish prior casting the MCC-dissolved solution (Figure 3.2b).

Regarding the obtained membranes, there is no uniform distribution of cork particles in the resulting membrane, which can be attributed to the hydrophobic behavior of cork particles in the presence of aqueous solutions. This non-uniform distribution of cork particles within the electrolyte is more pronounced in the membranes with lower amount of cork particles.

At a macroscopic level, the membranes prepared by method 1 exhibit significantly less brittleness compared to those obtained by method 2. This enhanced performance is attributed to the cork particles' ability to dissolve in the regeneration solution, facilitating a more stable and resilient integration into the electrolyte matrix.

In this context, it is worth noting that the approach of method 1 not only yields membranes that are less fragile at a macroscopic level but also ensures greater homogeneity in the incorporation of cork particles into the electrolyte matrix.

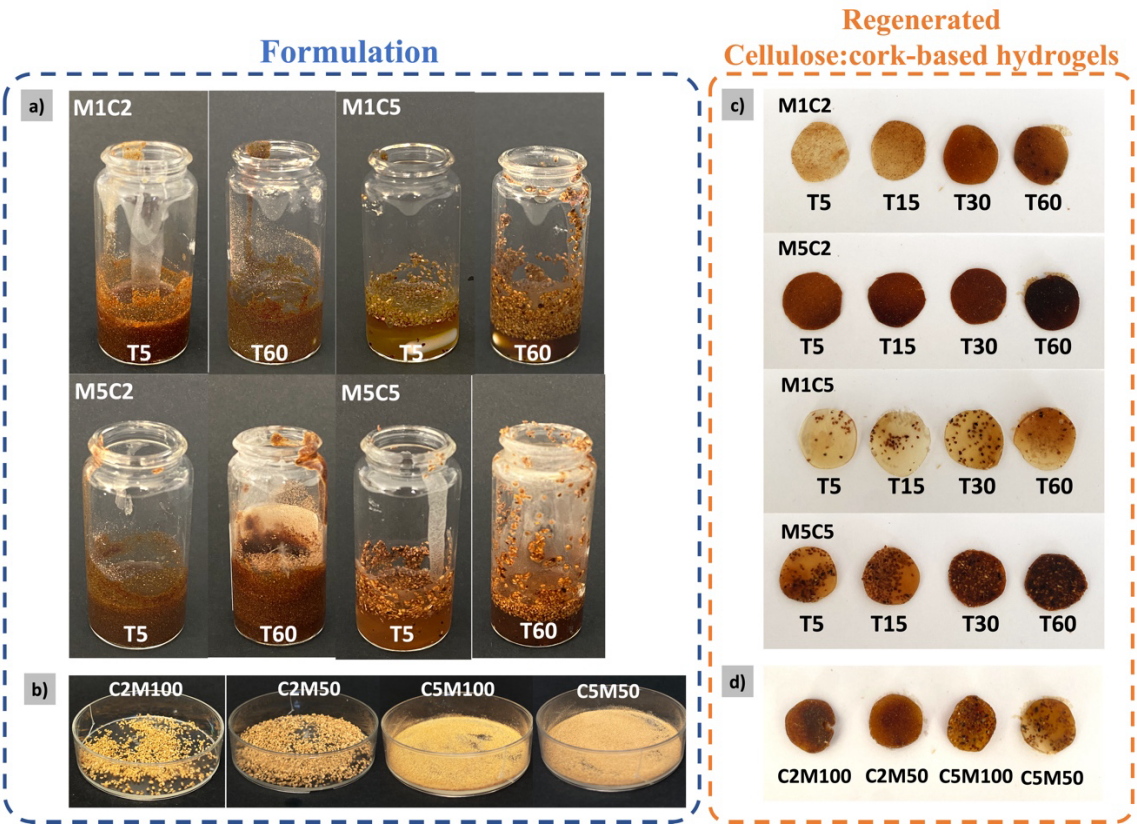

Figure 3.2 – Photography of the a) cellulose:cork-dissolved solution for 5 and 60 minutes, b) cork deposition after dropping the MCC-dissolved solution, regenerated cellulose:cork-based hydrogels obtained by c) method 1, and d) method 2.

3.2 Characterization of the electrolytes

3.2.1 Electrochemical characterization

EIS measurements were carried on the CE membranes, utilizing the capacitor configuration shown in. Figure 2.2a. A detailed study on the influence of the regeneration agent was done to find the optimal CE's composition that leads to best electrochemical performance.

Figure 3.3a-c show the variation of impedance and phase angle as a function of frequency for 4 replicas of the different electrolytes, with the corresponding Nyquist plots shown in Figure 3.3d. All results are documented in Table 5.3. The ionic conductivity of all the electrolytes was calculated using the expression (1) and represented in Figure 3.3e.

ECM electrolyte shows superior ionic conductivity at room temperature compared to the other two electrolytes obtained from different regeneration solution, reaching a value of 1.37 mS cm^{-1}. This result suggests that the use of a GAA:EG mixtures significantly favours the ionic conduction process. Pires and co-authors [18] reported ionic conductivity values of 7.85 $\times 10^{-5}$ mS cm^{-1} for PVA-H_3PO_4 as a solid−gel electrolyte. When this value is contrasted with the results obtained for cellulose-based electrolytes, a notable disparity emerges, with the conductivity of PVA-H_3PO_4 being considerably lower. Cellulose electrolytes, owing to their specific properties and higher ionic conductivity, are emerging as a more effective choice for electrochemical applications.

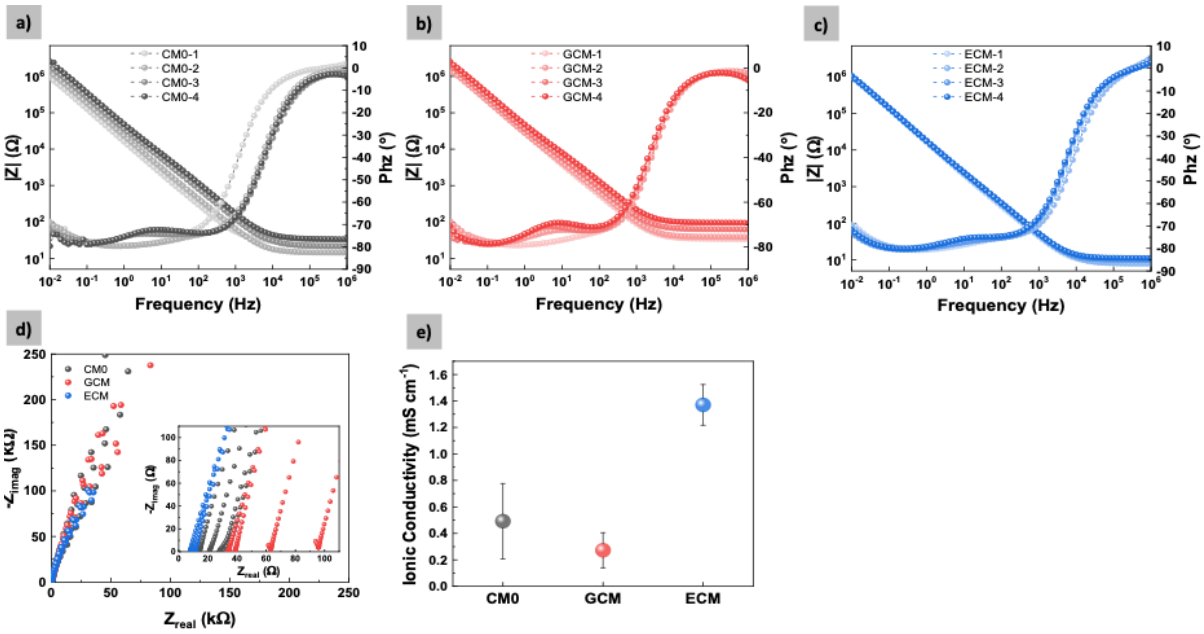

Figure 3.3 – a-c) Resistance and phase angle versus frequency plots of CM0, GCM and ECM, respectively. d) Plot of all Nyquist plots of CE. f) Plot of the ionic conductivities and respective standard error.

Figure 3.4 shows the ionic conductivity of the CCE samples, which are also listed in Table 5.4 and Table 5.5. The values shown reflect the mean and standard deviation, considering the three replicates of each electrolyte produced for the different methods under study.

Regarding the CCE membranes prepared by the method 1, the significant influence of size and weight concentration on the ionic conductivity of the electrolytes is evident. The variation in these factors not only underlines the sensitivity of the preparation method but also provides valuable insights for optimizing the ionic characteristics of CCE membranes, contributing to the advancement and improvement of electrochemical devices that incorporate them.

For a dissolution time of more than 30 minutes, there is a notable decrease in ionic conductivity in these specific membranes. This upward trend with dissolution time can be attributed to the fact that, as the particles are dissolved for a longer period in the cellulose solution, more uniform membranes are formed with lower bulk resistances.

It is also important to note that the variation in the ionic conductivity of membranes M1C5T60 and M5C2T60, in contrast to the general trend, may be influenced by specific factors such as the morphology of the cellulose particles used or the specific dissolution conditions. Further studies may be needed to fully understand the mechanisms underlying these variations. However, the consistent observation of a general increase in ionic conductivity with dissolution time suggests that optimizing the process could result in more efficient membranes for electrochemical applications.

On the other hand, it is clear that the ionic conductivity of the CCEs developed by method 2 is relatively low when compared to the values obtained for method 1. This disparity is attributed to the poor homogeneity present in the membranes produced by method 2, resulting from the inadequate incorporation of the cork particles into the cellulose solution. Another noteworthy aspect is the high bulk resistance, indicating impaired efficient ionic conduction within the membrane. These challenges in homogeneity and bulk resistance suggest the need to optimize method 2 in order to improve the quality and performance of CCE membranes, with the aim of achieving results closer to those obtained by method 1.

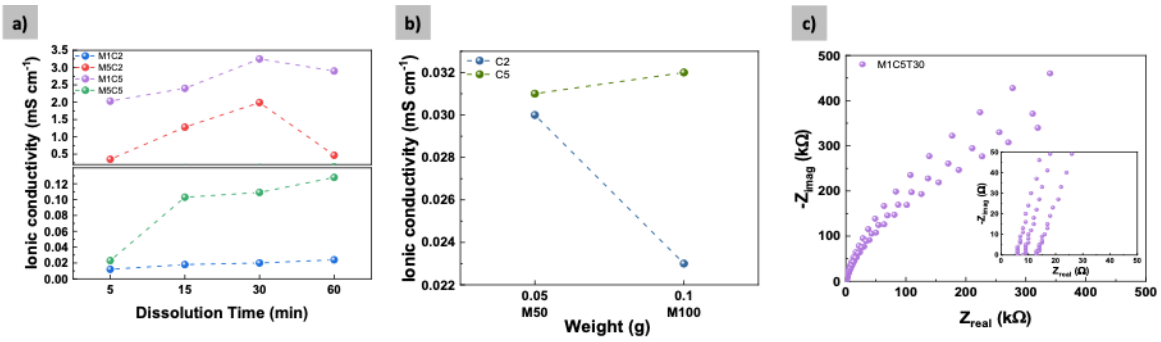

Figure 3.4 – a) Plot of the ionic conductivity of the CCEs (method 1) for different dissolution times. b) Plot of the ionic conductivity of CCEs (method 2) for different weights. c) Nyquist plot of the best CCE with 1wt.% of cork 500-800 µm, M1C5 (method 1).

Considering these results, the highest ionic conductivity values were obtained for M1C5T30 sample (3.37 mS cm^{-1}), when utilizing GAA:EG mixture as regenerating agent, and the ECM sample (1.37 mS cm^{-1}) using the same regenerating agents. Owing to their high ionic conductivity, they were selected for further studies and assessing their impact on the performance of SCs.

3.2.2 Thermal characterization

Figure 3.5 shows the thermal degradation of the selected electrolyte membranes, which starts with the desorption of moisture adsorbed in the cellulose-based matrix at temperatures below 70 ºC, followed by a steep weight loss up to nearly 200 ºC related to the thermal degradation of the composite material. The pronounced weight loss observed at low temperature corresponds to 16 and 25 % at 70 ºC for the M1C5T30 and ECM membranes, respectively, which corroborates their hydrogel character due to their ability to retain a high amount of weakly bonded water that is adsorbed in the cellulose network. This might influence the ionic conductivity of the electrolyte since we are losing water.

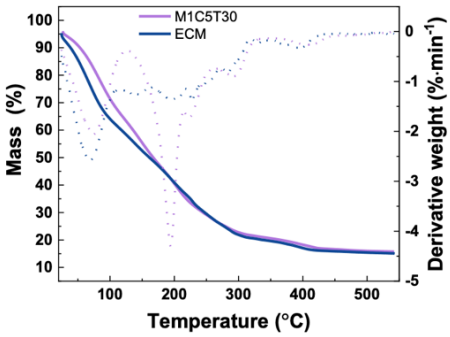

Figure 3.5 – TGA curves and respective derivatives (dotted lines).

3.2.3 Thermoelectrical characterization

The thermoelectrical behavior of both ECM and M1C5T30 electrolytes was study using a typical capacitor configuration as displayed on Figure 2.2. The capacitor was short-circuited for 5 minutes before being subjected to a thermal gradient. Then the open circuit thermovoltage (V_{OC}) was recorded for different temperature gradients ranging from 5 to 20 ºC, as illustrated in Figure 3.6a-b. The applied ΔT values were based on a previous work developed by L. Lochmatter [2], simulating the different temperature gradients that can be reached on the surface of the STB. The V_{OC} values were measured for 1000 s (~17 min). Figure 3.6a-b analyzes the variation in the open-circuit voltage (V_{OC}) of the ECM and M1C5T30 electrolytes in response to changes in temperature.

In Figure 3.6a, it is evident that the ECM electrolyte exhibits a loss of stability in V_{oc} after approximately 200 seconds when subjected to a ΔT higher than 10 ºC. This observation suggests potential challenges or limitations of the ECM under elevated thermal conditions. The decline in stability may be attributed to the loss of water with heating, decreasing the ionic conductivity of the electrolyte.

In contrast, as shown in Figure 3.6b, the M1C5T30 electrolyte shows a cumulative trend in V_{oc} values, indicating a positive and progressive response in the generation of electrical potential as the applied thermal gradient varies. This cumulative trend suggests that the electrolyte is capable of efficiently capturing and storing energy over time, and opens up the possibility of calculating the ionic Seebeck effect. This calculation is facilitated by obtaining the slope of a graph that represents the maximum V_{oc} values for different temperature gradients, as shown in the in Figure 3.6c. A maximum thermovoltage of ~ 43.18 mV is obtained for ΔT = 20 ºC after 1000 s. It is important to note that the ΔT value is monitored over time using the thermal camera. In this way, it can be concluded that V_{OC} stabilization occurs with the annulment of the thermal gradient.

Figure 3.6c reveals that the thermovoltage varies linearly with ΔT, resulting in an ionic Seebeck coefficient (S_i) of 2.04 mV K^{-1} for the M1C5T30 electrolyte determined by the [6]:

$$\Delta V_{\text{max.thermal}} = |S_i| \times \Delta T \quad (5)$$

The ability of the M1C5T30 electrolyte to demonstrate an efficient cumulative response, together with its propensity to facilitate the calculation of the ionic Seebeck effect, highlights it as a promising choice for TCSCs. On the other hand, the loss of stability observed in the ECM electrolyte, especially at thermal gradients greater than 10 ºC, suggests significant limitations for its application in TCSC, making the M1C5T30 a more advantageous option.

Pires and co-authors [38] reported values of 2.35 mV K^{-1} (ΔT = 20 K) for PVA-H_3PO_4 solid–gel electrolyte, and a maximum thermovoltage of ~45 mV is obtained. These values are very similar to the ones obtained in this work. Nevertheless, it is worth mentioning that the developed ECM and M1C5T30 were characterized in vertical configuration whereas the authors have conducted in the interdigital and planar configuration. Since a planar configuration will be able to provide higher thermoelectric potentials due to the existence of a relatively greater temperature gradient, as this is promoted by the greater distance between the hot and cold sides [6].

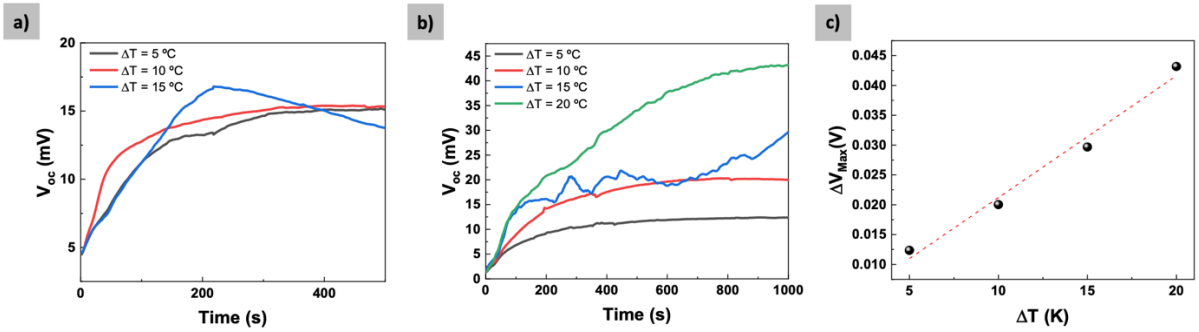

Figure 3.6 – Thermovoltage under open circuit measured over time for different ΔT (5, 10, 15, and 20 K) for: a) ECM; b) M1C5T30. c) ΔV maximum values as a function of ΔT, for M1C5T30.

3.3 Design and optimization of the fabricated supercapacitors on paper

Figure 3.7 shows a visual description of the process for developing the SCs, and Table 2.4 shows the list of the developed SCs using two different configurations.

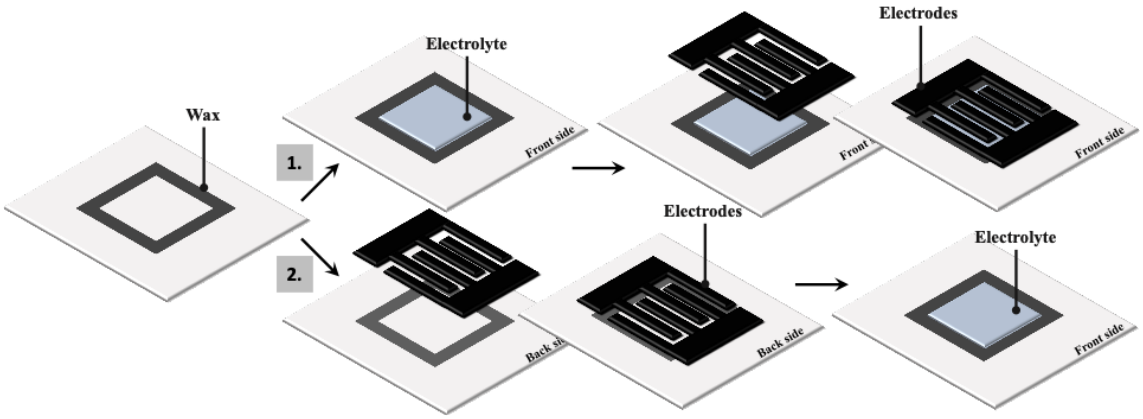

Figure 3.7 – Schematic representation of the TCSC's production process. 1. Corresponds to the first configuration adopted, with a paper/electrolyte/electrode structure; 2. Corresponds to the second configuration, this one with an electrode/paper/electrolyte structure.

Considering the configuration designs under focus, an initial study was performed to optimize the regeneration step using two distinct regeneration strategies: i) drop-casting the regeneration solvent mixture directly on the dissolved cellulose or soaking; ii) coating the dissolved cellulose solution with filter paper soakied in the regerenration solvent mixture. Figure 3.8 shows that the electrolytes have a more uniform surface when using soaked filter paper in the regenerative agent than those obtained by the drop casting method. This phenomenon is evidenced by the presence of circular patterns as droplets fall onto the solubilized cellulose solution, promoting abrupt and uneven regeneration along the electrolyte's surface. Therefore, the "soaking method" was the regeneration strategy adopted in the fabrication of the SCs.

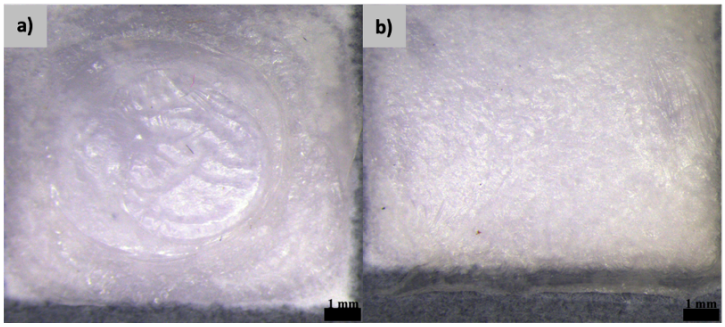

Figure 3.8 – Optical microscope images of ECM impregnation on paper by a) drop casting and b) soaking regeneration method.

Figure 3.9a-b shows the Nyquist plots for the ECM/paper electrolyte (obtained from soaking regeneration method), characterized in both controlled relative humidity (RH) conditions of 40 and 80 %, respectively, utilizing the capacitor configuration shown in. Figure 2.2a. Relevant parameters are listed in Table 3.4. It is possible to infer that higher humidity levels lead to a lower contact resistance. This is due to cellulose's ability to absorb water, promoting better ionic conductivity in more humid environments, values which are also proven by the ionic conductivity values obtained [40].

Comparing the ionic conductivity values obtained for the ECM membrane (1.37 mS cm^{-1}) at 40% humidity, it can be seen that the ECM/paper values, although lower, remain in the same order of magnitude (0.393 mS cm^{-1}) at 80% humidity. The lower ionic conductivity of the ECM/paper is expected since paper has been included in the electrolyte structure and hinders the movement of ionic species. Additionally, paper reinforces the structural mechanical integrity of the ECM and opens up other design possibilities for the SCs.

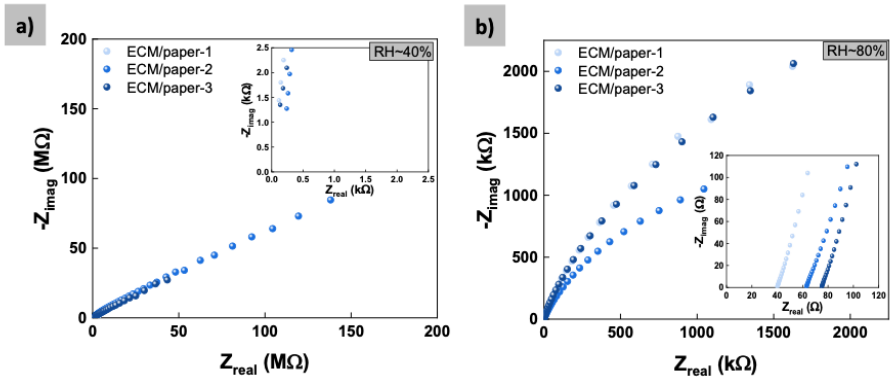

Figure 3.9 – a) Nyquist plots of ECM impregnated a) at ~40% RH and b) at ~80% RH.

Table 3.1 – Resume of the electrochemical characterization of the ECM/paper electrolytes. The values show the average and the respective standard error of the mean obtained from three samples each.

Sample Name	Thickness [mm]	$C_{f=100mHz}$ [µS·cm^{-2}]	R_b [Ω]	σ_i [mS·cm^{-1}]
ECM/paper (~40%)	0.383 ± 0.010	0.785 ± 1.164	1734.67 ± 580.97	0.013 ± 0.004
ECM/paper (~80%)		6.014 ± 1.732	59.41 ± 17.83	0.393 ± 0.143

Besides the electrolyte, electrodes are also a critical layer of the SCs. Current collectors in electrochemical devices must ideally combine high electrical conductivity, low contact resistance, electrochemical stability to prevent degradation over time, optimize charge transfer with good mechanical robustness, and establish an excellent interface with the active layers of the SCs as well as a good adhesion to prevent delamination during operation. In this work, we have selected a commercial, screen-printable, water-based carbon conductive ink to pattern the electrodes of the SCs. Its water-based formulation is not only economically and environmentally appealing but also non-toxic [41].

The effect of number of printed layers on paper on the electrical conductivity was studied (Figure 3.10). Ten samples were screen-printed with a square shape (active area of 1 cm^2) with different numbers of layers, ranging from 1 to 5, followed by annealing for 5 minutes at 100ºC. Keeping sheet resistance low is crucial for optimizing the performance and efficiency of the SCs.

Figure 3.10b shows that the sheet resistance decreases as the number of printing layers increases and stabilizes after three layers. As shown in the supplementary information, Figure 5.1, the uniformity of the pattern is achieved with only one printed layer, but the sheet resistance is still high. The optimum number of passes was three, resulting in a sheet resistance of 38.68 Ω sq^{-1}. In Figure 3.10, we can observe a topographical perspective of the screen-printed carbon film with three printing passes on paper, and the interface between the printed pattern and the paper, showcasing complete coverage of the printed design on paper, with the presence of repeated valleys which are related to transfer of the woven mesh pattern.

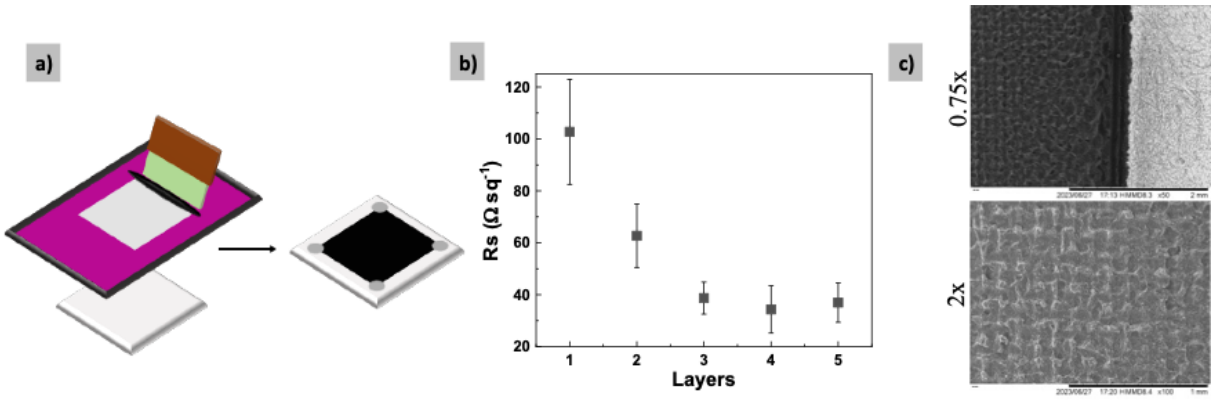

Figure 3.10 – a) Schematic of the screen-printing technique. b) Average sheet resistance (Rs) plots of the different samples. c) shows a SEM image of the interfaces between the paper and the carbon ink, at a magnification of 50 times and from the surface of the carbon, at a magnification of 100 times for 3 layers.

Considering the optimal procedure for the electrolyte and the electrodes, these strategies were implemented on the fabrication of the SCs. In Figure 3.11a-b, numerous imperfections are noticeable when the carbon ink is screen-printed on top of the electrolyte. These imperfections result in variations between the printing passages, compromising precise control over the interdigital fingers and preventing the formation of homogeneous conduction paths. In addition, poor contact between the electrodes and the electrolyte is evident, manifested by noticeable detachment with time and use. On the other hand, when the carbon electrodes and electrolyte are positioned on opposite sides of the paper, both exhibit greater uniformity in their implementation, as depicted in Figure 3.11c-d, respectively.

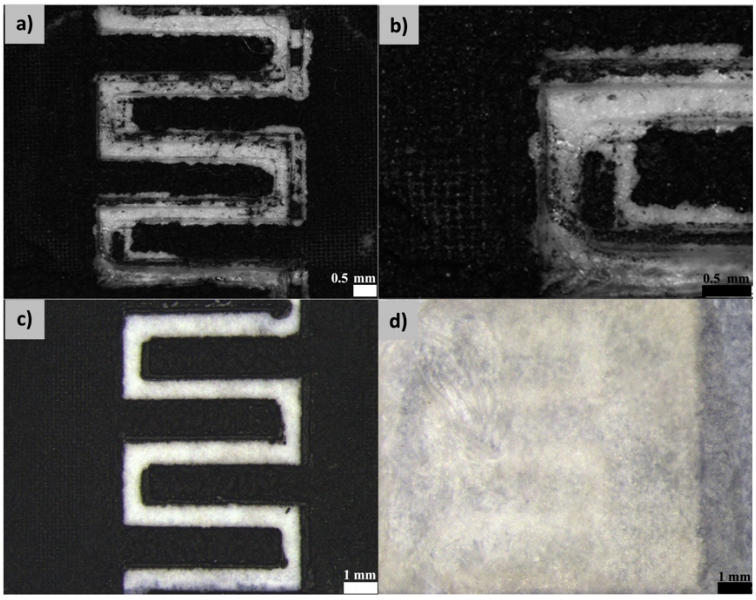

Figure 3.11 – Leica images. a) and b) Paper/electrolyte/electrodes configuration (TE SC). Electrode/paper/electrolyte configuration (BE SC) from c) back side with electrodes and d) front side with the electrolyte.

Regarding the configuration designs studied, one of the crucial challenges in the manufacture of SCs is ensuring a smooth interface between all the materials involved. Considering this challenge, a strategic decision was made to avoid manufacturing the SCs directly on the membranes, given their sensitivity to humidity, which could cause deformation of the deposited layers. This precaution is motivated by the behavior of the electrolyte, which adjusts its dimensions in response to the amount of water retained, varying according to humidity conditions.

On the other hand, Configuration 2 ensures an efficient interface between the various deposited layers that interact with the electrolyte, impregnating the paper with the final. From this perspective, the paper/electrolyte will fulfill the role of the electrolyte as a whole.

3.4 Characterization of the fabricated supercapacitors

The electrochemical characterization of the developed SCs started with impedance analysis at two different relative humidity values. In a previous work, Carvalho et al. [40] have shown the influence of the RH on fiber-shaped supercapacitors integrating a cellulose hydrogel electrolyte. Higher RH levels led to a decrease in the contact resistance, and additionally resulted in higher specific capacitance and energy density. Therefore, before starting the full electrochemical characterization of the SCs, their humidity susceptibility was evaluated by placing them in an environment with controlled humidity at ~80% for 12 hours and then 12 hours at an RH of ~40%.

As displayed in Figure 3.12, the impedance was recorded at 1 kHz for 24 hours showing the high susceptibility of the SCs to humidity variation. TE, BE and BEC SCs exhibited equivalent series resistance (ESR) in order of 500 Ω, and these values remained stable for 12 h at RH ~of 80 %. However, as soon as the RH changes the impedance increases, reaching values of 3, 2.5, and 1.75 kΩ, respectively, after 12 h at RH of 40 %.

The SCs with ECM displays a more pronounced increase in impedance compared to the SC with M1C5T30, in the first hours at 40 % of RH. This can be related to the addition of cork particles which may decrease the hydrophilicity of the electrolyte system.

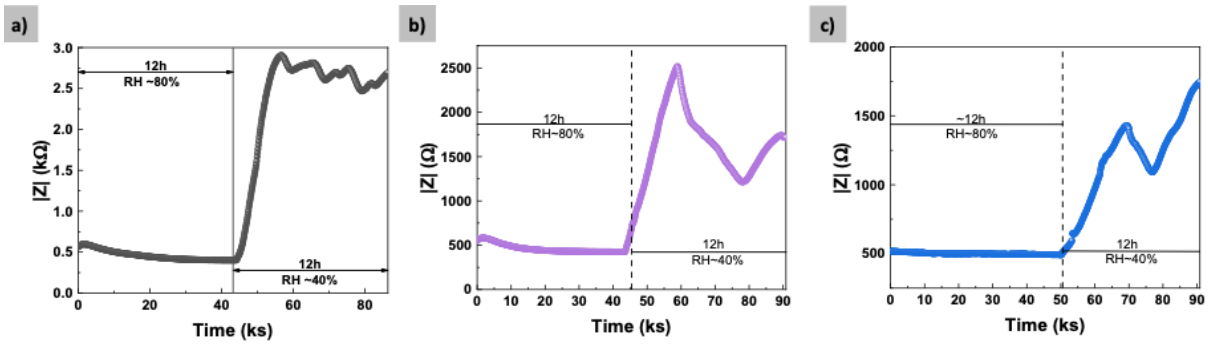

Figure 3.12 – Impedance plot acquired at 1kHz, during 24h with different ambient conditions for the developed SCs: a) TE SC (ECM electrolyte). b) BE SC (ECM electrolyte) and, c) BEC SC (M1C5T30 electrolyte).

Taking this into consideration, the electrochemical performance of the SCs was evaluated by CV, GCD, and EIS in a two-electrode cell configuration to unveil their energy storage properties.

CV and GCD analyses were performed to determine the appropriate operating voltage window (OVW) of the devices, as well as determine the specific storage capacitance (C_s). CV was first assessed to determine the safe OVW by gradually increasing the voltage, as displayed in Figure 3.13. Therefore, 0.8 V was the selected as a stable OVW to conduct the further electrochemical analysis, without carrying the risk of further develop reactions that might hinder the devices performances. As previously mentioned, hydrogel electrolytes have limited OVW owing to the presence of water in their constitution.

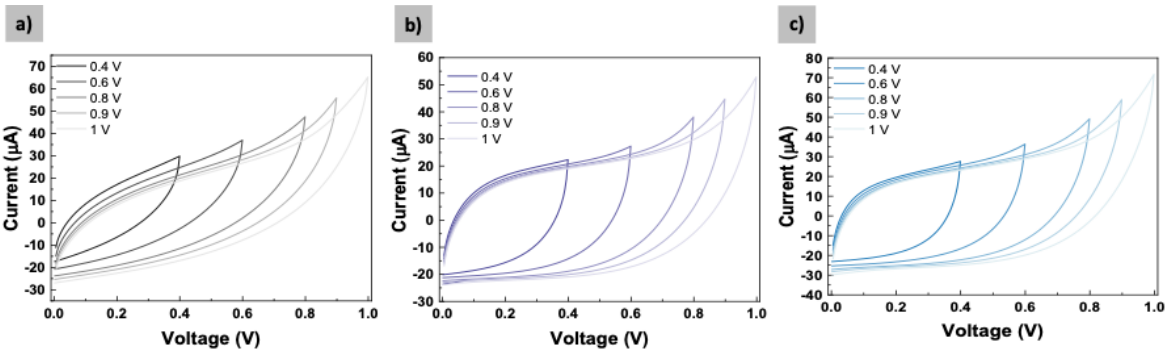

Figure 3.13 – Cyclic Voltammograms performed at 10 mV s^{-1}, to study the evolution of the stable operation voltage window, for TE, BE and BEC, respectively.

Figure 3.14b,e,h exhibits the i−V cycles at different scan rates from 5 to 500 mV s^{-1} in the voltage window between 0 and 0.8 V. A non-faradaic electrostatic charge storage mechanism was detected on both devices due to the quasi-rectangular curve shape of the cyclic voltammograms, which is typical of EDLCs, where carbon-based materials are used as active materials.

Figure 3.14c,f,i exhibits GCD curves at different scan rates from 10 to 300 μA cm^{-1}. It is possible to observe that present a triangular curve shape, characteristic of EDLCs.

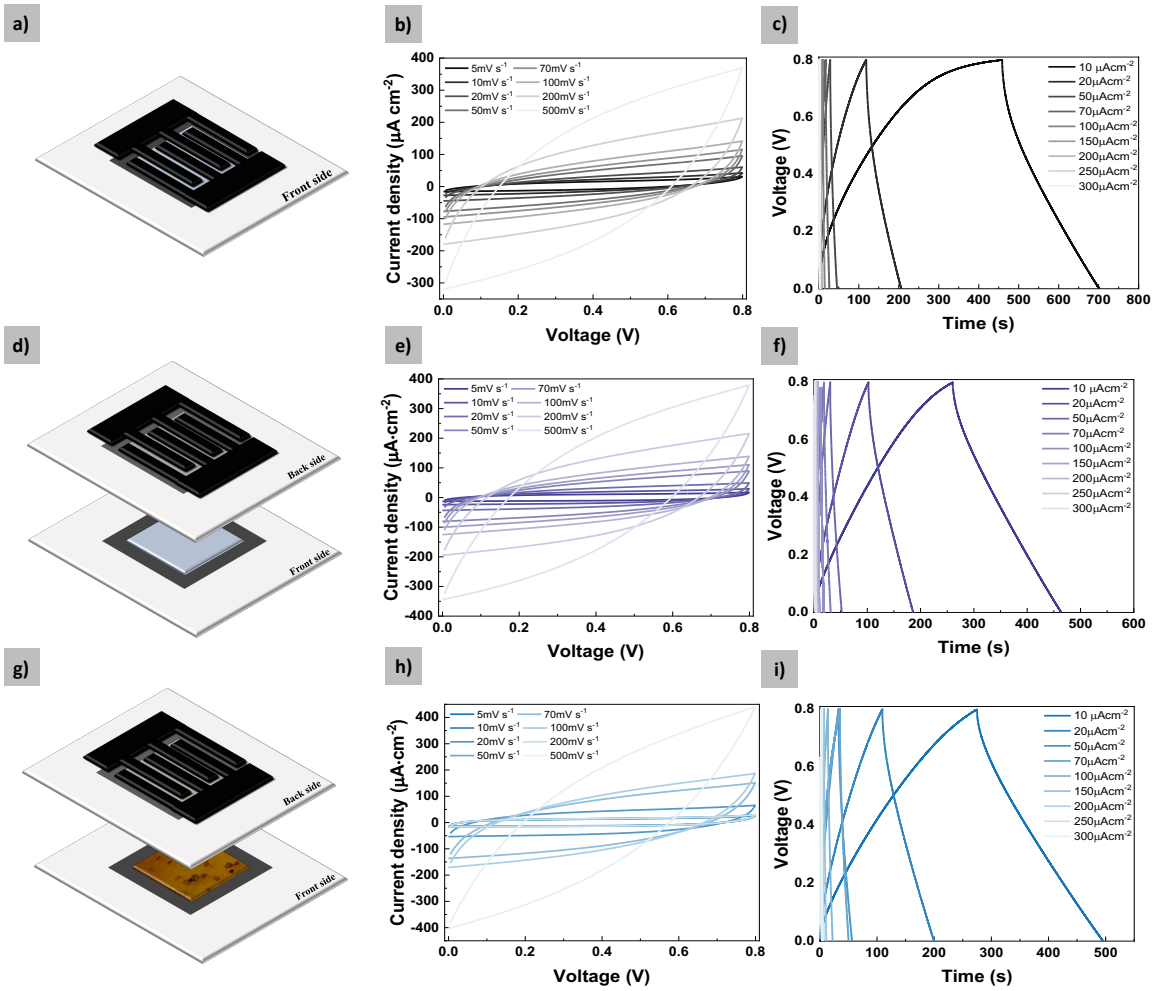

Figure 3.14 – Electrochemical characterization: a,d,f) Schematic representation of the TE SC, BE SC and BEC SC, respectively; b,e,h) CV cycles measured at different scan rates for TE SC, BE SC and BEC SC, respectively; c,f,i) GCD curves at different current densities for TE SC, BE SC and BEC SC, respectively.

The C_s of the devices was determinate from CV and GCD measurements (Figure 3.15a-b and Table 5.**6**), through expression (1). In Figure 3.15a-b is depicted the variation of the C_s determined from CV and GCD measurements as a function of the scan rate and current density, respectively. It is possible to observe that the C_s decreases upon the increase in the scan rate and current density. This variation is related to the shorter time for the formation of the EDL at higher scan rates, while at lower scan rates the electrolyte ions have more time to accommodate in the pores of the electrodes.

The C_s of all the electrochemical characterized SCs using both configurations and the different electrolytes, TE, BE and BEC, at a scan rate of 10 mV s^{-1}, is in the order of magnitude mF cm^{-2}. Maximum C_s values of 1.80, 1.78 and 2.63 mF cm^{-2} were achieved at a scan rate of 5 mV s^{-1}, for TE, BE, and BEC SCs, respectively, while for a scan rate of 10 µA cm^{-1} C_s values correspond to 3.08, 2.58 and 3.38 mF cm^{-2} for TE, BE and BEC SCs, respectively. Comparing the values obtained for the different SCs, it can be seen that BEC SC exhibit a superior C_s value, owing to the superior ionic conductivity of the M1C5T30 electrolyte.

The C_s values obtained for the fabricated SCs are slightly higher in comparison with those presented in the literature for interdigital SCs. Pires and co-authors [18] reported C_s values of 0.95 mF cm^{-2} for multi-walled carbon nanotubes-based (MWCNT) electrodes using PVA-H_3PO_4 as a solid−gel electrolyte.

Using equations (2) and (3), a maximum energy density of 0.272, 0.227, and 0.298 µWh cm^{-2} was obtained and a maximum power density of 0.206, 0.474, and 0.329 mW cm^{-2} for TE, BE, and BEC SCs, respectively, as shown in Figure 3.15c. The achieved outputs are promising, although slightly inferior to the results reported in the literature. Pires and co-authors [18] reported power values of 0.97 mW cm^{-2} and energy values of 0.84 µWh cm^{-2}.

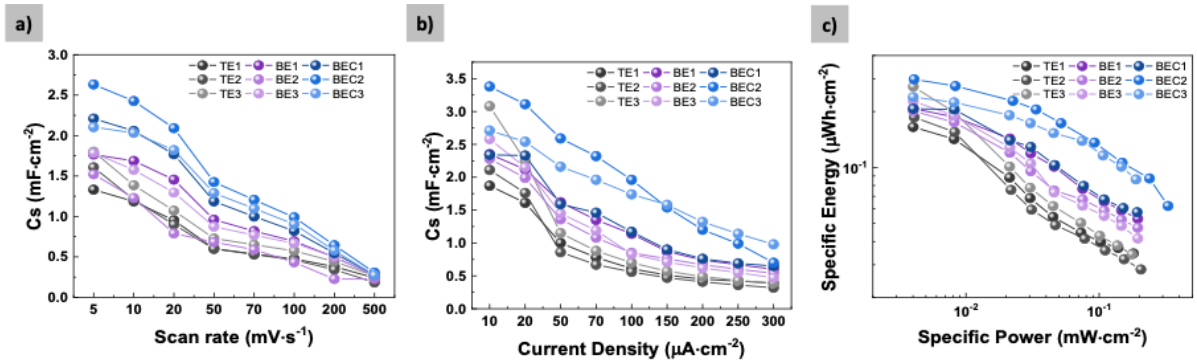

Figure 3.15 – Electrochemical characterization of all the devices: a) Variation of the specific capacitance as a function of the scan rate. b) Variation of the specific capacitance as a function of the current density. c) Specific energy as a function of the specific power.

EIS measurements were performed to understand the type of energy storage mechanism and determine the ESR. As depicted in Figure 3.16a, the Nyquist plot shows that the electrode behavior strongly depends on the frequency. ESRs of 439, 688 and 573 Ω are obtained for TE, BE, and BEC SCs, which are similar to the internal resistance extracted at 1 kHz.

In Figure 3.16b-c are presented the cycling stability test of the devices BE and BEC SCs during 10000 charge/discharge cycles at 200 mV s^{-1}. The devices exhibit a capacitance retention of 114% and 143% respectively, confirming its excellent cyclability. Furthermore, an increase of the last curve was observed when compared to the first i-V curve. This is not a common behavior reported in the literature but has been observed in different materials. This could be related of the electrodes nanostructure adaptation to the system, the electrolyte wettability which can lead to an increase in capacitance retention. [42]

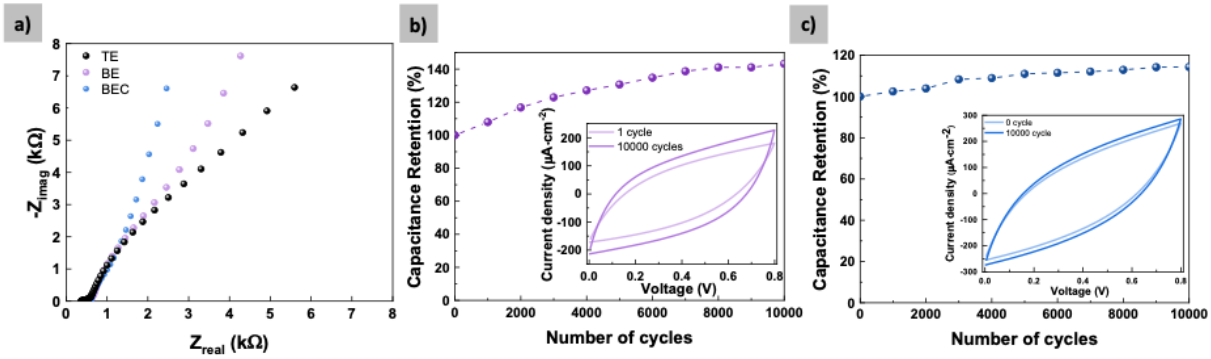

Figure 3.16 – Electrochemical characterization of all the devices. a) Nyquist plot obtained from EIS measurements. b) Cycling stability test during 10000 charge/discharge cycles for BE3. c) Cycling stability test during 10000 charge/discharge cycles for BEC1. The insets of b-d show the first and the last i−V cycles of the devices.

Flexibility is also important for the fabrication of SCs. Therefore, we have conducted mechanical bending tests to evaluate the mechanical endurance of the developed SCs. Using a custom-made bending machine bending (Figure 3.17a), 1000 bending cycles were performed. Figure 3.17b-c shows the CVs before and after subjecting the devices to the mechanical stress for BE and BEC SCs, respectively. A slightly decrease in the area of the CVs was verified after bending. This reflects in the capacitance decrease that might be associated with some degradation of the printed interdigitated carbon electrodes, as well as detachment of the same or even the ECM and M1C5T30 electrolytes, respectively. It is also important to mention that this mechanical bending and subsequent electrochemical characterization was conducted in a non-controlled environment. Therefore, we cannot discard the fact that changes in the humidity can impact the performance of the SCs, owing to the hydrophilic nature of the developed electrolytes.

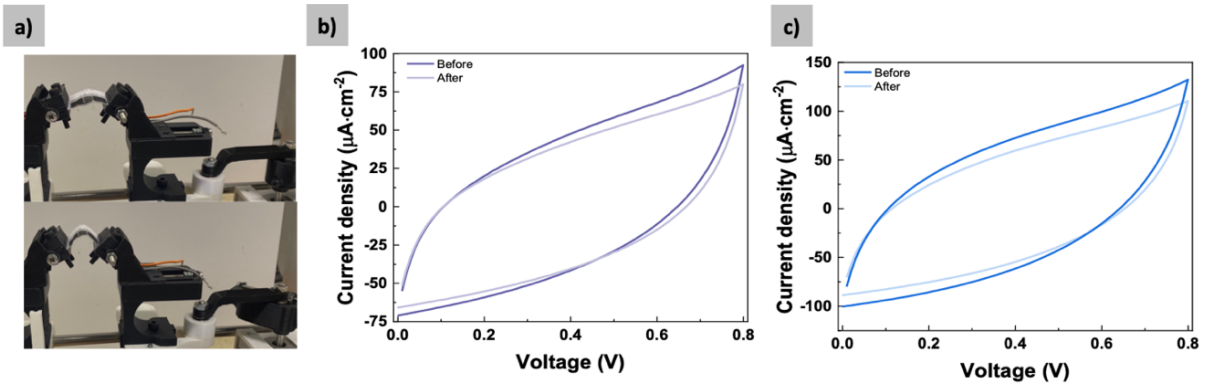

Figure 3.17 – a) Photographs of the TCSCs in flat and bent positions. The respective CVs before and after the 1000 bending cycles, (mVs^{-1}): using b) ECM; c) M1C5T30 as electrolytes.

The scalability of the developed SCs was demonstrated by connecting in series six printed SCs, using the configuration 2 and ECM as the electrolyte. Briefly, three-layered carbon electrodes were screen-printed on paper with planar interdigitated design. Then silver SInk01NP ink, NanoPaint, was used to create the interconnection pathways, as shown in Figure 3.18a. Subsequently, the ECM electrolyte was drop-casted and regenerated on the back side (Figure 3.18b).

The six TSCS connected in series were charged with 4.8 V and connected to a wristwatch. Figure 3.18c shows that not only is it possible to turn on the watch, but that it can stay on for around 4 minutes.

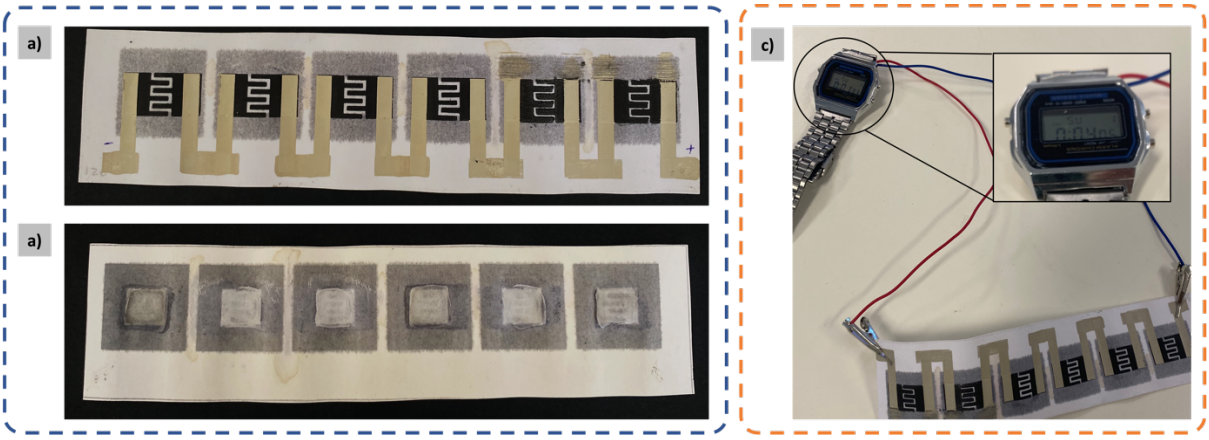

Figure 3.18 – Photographs of a) the six printed TS-SCs in serie. b) the ECM electrolyte impregnated. c) the operating device, the inset shows the clock's last operating time.

3.5 Proof-of-concept: thermally chargeable supercapacitors

Based on the studies carried out in 3.2, it was found that the electrolyte containing cork particles has promising characteristics for its application in TCSC. By combining the promising thermoelectric properties of the selected electrolyte (M1C5T30) with the high capacitive performance of the SCs produced with planar interdigital carbon electrodes, we demonstrate the operation of the TCSCs. The ionic thermoelectric effect acts as an internal electrical generator, charging the SC's EDLC.

Figure 3.19 illustrates the charge/discharge cycle obtained for the TCSC produced. The states shown (1) initial state, (2) charging, (3) storage, and (4) discharging correspond to the four states proposed by the electrochemical operating mechanism shown in Figure 1.5, demonstrating the TCSC concept [18].

Immediately before the start of state 1, the electrolyte ions are randomly distributed in the electrolytic medium. When ΔT = 20 ºC is applied to the TCSCs (1), the electrolyte cations migrate to the cold electrode due to the Soret effect, leading to an increase in voltage (V_{thermo}) until it reaches a stable value of around 3.04 mV. Then, when $R_{Load\ =\ 100\ k\Omega}$ is turned on, the charging state (2) begins, in which the voltage (V_{Load}) decreases rapidly, reaching a stable value of around 0.57 mV. It would be expected that at the end of state 2), the voltage would gradually drop to ≈0 V as the amount of accumulated ions reaches their maximum concentration. However, this does not happen due to the residual voltage, which is associated with electronic leakage current, resulting in a non-zero voltage drop after the TCSC has been fully charged [20].This curve corresponds to the device's charging curve, and the abrupt decrease in V_{Load} during charging is due to the transfer of charge to the capacitor, inducing an opposite signal compensated by the thermovoltage. The effective charging voltage ($V_{effective}$) is around 2.47 mV. Once the TCSC is fully charged, heating is turned off, and R_{Load} is removed (3), the circuit is reopened, allowing charges to be transferred to the TCSC electrodes. This causes the voltage (V_{thermo}) to drop to negative values until it stabilizes, inducing the TCSC to charge again. In state 4), the TCSC is discharged by introducing R_{Load}, which unbalances the ions in the electrolyte, generating an electric current in the external circuit and causing the random migration of cations into the electrolytic medium. The introduction of R_{Load} simulates the external device intended to be powered with the energy converted during the discharge of the TCSC, thus transforming the accumulated energy into a useful form for the operation of an electronic device

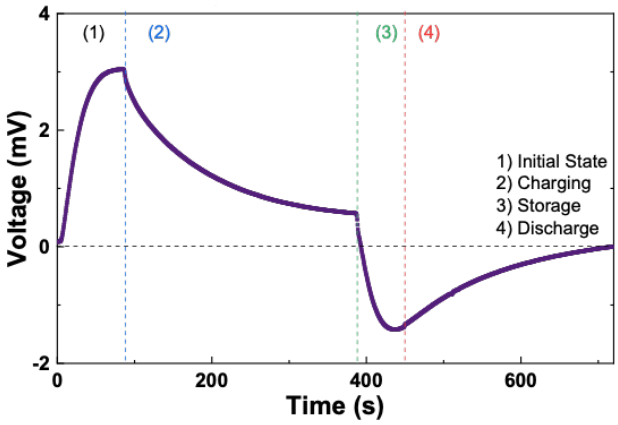

Figure 3.19 – Voltage curve of the TCSC device as a function of time when a temperature gradient ΔT = 20 K is applied.

Finally, the energy storage obtained through the thermal gradient was determined using Equation (2), considering the effective charging voltage of the device for ΔT = 20 ºC (Figure 3.19), resulting in an E of ~2.55 pW h cm^{-2}, which corresponds to a charge on the electrodes, Q_{ch} of 0.12 mC cm^{-2} determined through the following equation:

$$Q_{ch} = C(S_i \times \Delta T) \quad (5)$$

Pires and co-authors [18] reported values of ~118 nWh cm^{-2} for E and 128 mC cm^{-2} for Q_{ch}, of MWCNT based electrodes using PVA-H_3PO_4 as a solid−gel electrolyte. The thermoelectric measurements show considerable differences, since they were carried out for a ΔT = 20 ºC, while the authors performed the characterization for a ΔT = 10 ºC. It is understandable that there is a disparity in the values obtained due to this variation in experimental conditions.

Another factor to consider is that the measurements require a humidity-controlled environment, a condition that is difficult to maintain when applying temperature to the TSCS. This challenge points to the need to encapsulate the device, ensuring ideal humidity conditions to optimize the performance of the electrolyte.

Despite the differences from literature values, the results achieved by the proposed TCSC prototype offer a promising solution for integrating energy conversion and storage into a single device. This highlights the system's potential ability to harness the residual heat from an STB after proper optimization, converting it into electrical energy and storing it for later use as an external energy source to power electronic alarm devices.

4

CONCLUSIONS & FUTURE PERSPECTIVES

In this work, we developed a thermally chargeable supercapacitor (TCSC) with an interdigital planar configuration on a paper substrate suitable for flexible applications. Screen printing was the selected technique to design the commercial carbon water-based ink as active material and current collector.

Efforts were made to develop an electrolyte composed of sustainable materials from natural sources, such as cellulose and cork, to power future electronic devices. A thorough analysis of the electrolyte formulation was conducted, which was produced using an aqueous cellulose dissolution method at low temperatures. The impact of the regeneration agent as well as the incorporation of cork particles, were investigated in terms of conformability and ionic conductivity. The utilization of a GAA:EG mixture, as regenerating agent, proved effective in achieving a higher ionic conductivity value. Additionally, incorporating 1wt.% of cork particles (500-800 μm) into the cellulose electrolyte and dissolving them in the solution for 30 minutes resulted in a slight increase in the ionic conductivity of the hydrogel, from 1.37 to 3.25 mS cm^{-1}. It was possible to confirm a robust thermoelectric performance in the electrolyte containing cork, with an ionic Seebeck coefficient value of 2.04 mV K-1, reaching approximately ~ 43.18 mV in an open circuit for a thermal gradient of 20 K.

The development of the SCs prototype encountered significant challenges in achieving the harmonious integration between the electrolyte and electrodes. Because the cellulose electrolyte did not display the required adhesion to the carbon electrodes when placed in direct contact, we found that the most appropriate approach was to position them on opposite sides of the substrate, thus ensuring efficient contact with the paper.

Regarding the SCs performance, the cellulose:cork electrolyte enabled the achievement of a Cs of 2.21 mF cm^{-2}, surpassing the recorded Cs of 1.78 mF cm^{-2} for the cellulose electrolyte. These values slightly exceed those reported in comparable studies in the literature. After undergoing 10000 CV cycles, the SCs utilizing both electrolytes exhibited an impressive retention capacitance, remaining consistently above 100%. Furthermore, even after 1000 bending cycles, despite the device's capacitance slight decrease, it remained within the same order of magnitude. These results underscore the remarkable stability and durability of the SCs over time and under bending conditions, highlighting the robustness of the system.

The practical application of the developed SCs was validated, initially, by the interconnection in series of 6 devices to power a wristwatch for approximately 4 minutes, showcasing its ability to deliver sustainable and efficient energy for real-world applications.

A successful test confirmed that the TCSCs with cellulose:cork electrolyte can be charged using a thermal gradient of 20ºC, reaching a maximum thermovoltage of 2.47 mV. In addition, the discharge capacity was demonstrated by supplying current to an external circuit. These results underline the

potential use of the TCSCs as power supply devices for warning devices to keep consumers informed about the STB's thermal status.

The future development of the TCSCs must consider their applicability and seek improvements in its performance. One of the most significant points of interest is the study, of implementing a new configuration that can provide better thermoelectric values, with the aim of further differentiating the performance levels of TSCS. The comparison between planar and vertical structures might be relevant to determine which one is the most appropriated to satisfy the intended application and harvest the wasted heat and use it to power the device. This choice is not only based on the approximately 20 times higher thermovoltage values obtained during the characterization of the M1C5T30 electrolyte in this type of configuration compared to the planar structure used for the SCs, but also takes into account studies reported in the literature that highlight the benefits of this specific configuration [13], [43].

The encapsulation of the TCSCs must be considered, especially considering that the electrolyte is cellulose-based – a material highly susceptible to variations in humidity and temperature. Given the temperature-dependent nature of these devices, the encapsulation stage is of utmost importance and can yield improvements in reliable/stable performance.

5 REFERENCES

[1] C. C. Lee and P. S. Lam, “Critical Study on the Relationship between Power Conversion Technique and Energy Efficiency on Set-top Box.” [Online]. Available: https://www.gov.hk/tc/theme/bf/consultation/pdf/10111_consultation_pa

[2] L. Lochmatter “Energetically Autonomus Thermochromic Smart Tags”, 2022.

[3] “Policy Briefs in support of the high-level political forum leveraging energy action for advancing the sustainable development goals.” [Online]. Available: https://sustainabledevelopment.un.org/contact

[4] X. Shan *et al.*, “Wood for Application in Electrochemical Energy Storage Devices,” *Cell Rep Phys Sci*, vol. 2, no. 12, p. 100654, 2021, doi: 10.1016/j.xcrp.2021.100654.

[5] H. Chen *et al.*, “Exploring Chemical, Mechanical, and Electrical Functionalities of Binders for Advanced Energy-Storage Devices,” *Chem Rev*, vol. 118, no. 18, pp. 8936–8982, 2018, doi: 10.1021/acs.chemrev.8b00241.

[6] J. S. Teixeira, R. S. Costa, A. L. Pires, A. M. Pereira, and C. Pereira, “Hybrid dual-function thermal energy harvesting and storage technologies: Towards self-chargeable flexible/wearable devices,” *Dalton Transactions*, vol. 50, no. 29, pp. 9983–10013, 2021, doi: 10.1039/d1dt01568k.

[7] L. Wei, M. Wu, M. Yan, S. Liu, Q. Cao, and H. Wang, “A Review on Electrothermal Modeling of Supercapacitors for Energy Storage Applications,” *IEEE J Emerg Sel Top Power Electron*, vol. 7, no. 3, pp. 1677–1690, 2019, doi: 10.1109/JESTPE.2019.2925336.

[8] A. Tyagi, K. M. Tripathi, and R. K. Gupta, “Recent progress in micro-scale energy storage devices and future aspects,” *J Mater Chem A Mater*, vol. 3, no. 45, pp. 22507–22541, 2015, doi: 10.1039/c5ta05666g.

[9] H. Wang *et al.*, “Ionic Thermoelectric Figure of Merit for Charging of Supercapacitors,” *Adv Electron Mater*, vol. 3, no. 4, Apr. 2017, doi: 10.1002/aelm.201700013.

[10] J. Zhao, Y. Gao, and A. F. Burke, “Performance testing of supercapacitors: Important issues and uncertainties,” *J Power Sources*, vol. 363, pp. 327–340, 2017, doi: 10.1016/j.jpowsour.2017.07.066.

[11] J. Liu *et al.*, “Advanced Energy Storage Devices: Basic Principles, Analytical Methods, and Rational Materials Design,” *Advanced Science*, vol. 5, no. 1, 2018, doi: 10.1002/advs.201700322.

[12] C. Liu, X. Yan, F. Hu, G. Gao, G. Wu, and X. Yang, “Toward Superior Capacitive Energy Storage: Recent Advances in Pore Engineering for Dense Electrodes,” *Advanced Materials*, vol. 30, no. 17, pp. 1–14, 2018, doi: 10.1002/adma.201705713.

[13] S. L. Kim, H. T. Lin, and C. Yu, “Thermally Chargeable Solid-State Supercapacitor,” *Adv Energy Mater*, vol. 6, no. 18, Sep. 2016, doi: 10.1002/aenm.201600546.

[14] M. Haque *et al.*, “Exploiting low-grade waste heat to produce electricity through supercapacitor containing carbon electrodes and ionic liquid electrolytes,” *Electrochim Acta*, vol. 403, Jan. 2022, doi: 10.1016/j.electacta.2021.139640.

[15] A. Phalak, “Thermally charging capacitor: A new protocol to accurately measure the thermoelectric potential,” 2022.

[16] H. Jia, X. Tao, and Y. Wang, “Flexible and Self-Healing Thermoelectric Converters Based on Thermosensitive Liquids at Low Temperature Gradient,” *Adv Electron Mater*, vol. 2, no. 7, Jul. 2016, doi: 10.1002/aelm.201600136.

[17] P. Forouzandeh, V. Kumaravel, and S. C. Pillai, “Electrode materials for supercapacitors: A review of recent advances,” *Catalysts*, vol. 10, no. 9, pp. 1–73, 2020, doi: 10.3390/catal10090969.

[18] A. L. Pires, R. S. Costa, C. Pereira, and A. M. Pereira, “An Interdigital Planar Energy Harvesting/Storage Device Based on an Ionic Solid-Gel Polymer,” *ACS Appl Electron Mater*, vol. 3, no. 2, pp. 696–703, Feb. 2021, doi: 10.1021/acsaelm.0c00853.

[19] X. Yang *et al.*, “High-Performance Ionic Thermoelectric Supercapacitor for Integrated Energy Conversion-Storage,” *Energy and Environmental Materials*, vol. 5, no. 3, pp. 954–961, Jul. 2022, doi: 10.1002/eem2.12220.

[20] D. Zhao *et al.*, “Ionic thermoelectric supercapacitors,” *Energy Environ Sci*, vol. 9, no. 4, pp. 1450–1457, Apr. 2016, doi: 10.1039/c6ee00121a.

[21] R. Martins *et al.*, “Papertronics: Multigate paper transistor for multifunction applications,” *Appl Mater Today*, vol. 12, pp. 402–414, Sep. 2018, doi: 10.1016/j.apmt.2018.07.002.

[22] J. T. Carvalho *et al.*, “Fully printed zinc oxide electrolyte-gated transistors on paper,” *Nanomaterials*, vol. 9, no. 2, Feb. 2019, doi: 10.3390/nano9020169.

[23] N. Zavanelli and W. H. Yeo, “Advances in Screen Printing of Conductive Nanomaterials for Stretchable Electronics,” *ACS Omega*, vol. 6, no. 14. American Chemical Society, pp. 9344–9351, Apr. 13, 2021. doi: 10.1021/acsomega.1c00638.

[24] Y. Gao *et al.*, “Printable electrode materials for supercapacitors,” *ChemPhysMater*, vol. 1, no. 1. Elsevier B.V., pp. 17–38, Jan. 01, 2022. doi: 10.1016/j.chphma.2021.09.002.

[25] M. G. Say *et al.*, “Scalable Paper Supercapacitors for Printed Wearable Electronics,” *ACS Appl Mater Interfaces*, vol. 14, no. 50, pp. 55850–55863, Dec. 2022, doi: 10.1021/acsami.2c15514.

[26] F. Brunetti *et al.*, “Printed Solar Cells and Energy Storage Devices on Paper Substrates,” *Advanced Functional Materials*, vol. 29, no. 21. Wiley-VCH Verlag, May 23, 2019. doi: 10.1002/adfm.201806798.

[27] E. M. Materon *et al.*, “Combining 3D printing and screen-printing in miniaturized, disposable sensors with carbon paste electrodes,” *J Mater Chem C Mater*, vol. 9, no. 17, pp. 5633–5642, May 2021, doi: 10.1039/d1tc01557e.

[28] I. Cunha, “Printed and drawn flexible electronics based on cellulose nanocomposites,” 2021.

[29] S. Khan, L. Lorenzelli, and R. S. Dahiya, “Technologies for printing sensors and electronics over large flexible substrates: A review,” *IEEE Sens J*, vol. 15, no. 6, pp. 3164–3185, Jun. 2015, doi: 10.1109/JSEN.2014.2375203.

[30] A. T. Vicente *et al.*, “Multifunctional cellulose-paper for light harvesting and smart sensing applications,” *Journal of Materials Chemistry C*, vol. 6, no. 13. Royal Society of Chemistry, pp. 3143–3181, 2018. doi: 10.1039/c7tc05271e.

[31] D. Trache *et al.*, “Microcrystalline cellulose: Isolation, characterization and bio-composites application—A review,” *International Journal of Biological Macromolecules*, vol. 93. Elsevier B.V., pp. 789–804, Dec. 01, 2016. doi: 10.1016/j.ijbiomac.2016.09.056.

[32] X. Qi, Y. Zhang, C. Chang, X. Luo, and Y. Li, “Thermal, Mechanical, and Morphological Properties of Rigid Crude Glycerol-Based Polyurethane Foams Reinforced With Nanoclay and Microcrystalline Cellulose,” *European Journal of Lipid Science and Technology*, vol. 120, no. 5, May 2018, doi: 10.1002/ejlt.201700413.

[33] D. Trache *et al.*, “Microcrystalline cellulose: Isolation, characterization and bio-composites application—A review,” *International Journal of Biological Macromolecules*, vol. 93. Elsevier B.V., pp. 789–804, Dec. 01, 2016. doi: 10.1016/j.ijbiomac.2016.09.056.

[34] B. El Allaoui, H. Benzeid, N. Zari, A. el kacem Qaiss, and R. Bouhfid, “Functional cellulose-based beads for drug delivery: Preparation, functionalization, and applications,” *Journal of Drug Delivery Science and Technology*, vol. 88. Editions de Sante, Oct. 01, 2023. doi: 10.1016/j.jddst.2023.104899.

[35] M. Oprea and S. I. Voicu, “Recent advances in composites based on cellulose derivatives for biomedical applications,” *Carbohydrate Polymers*, vol. 247. Elsevier Ltd, Nov. 01, 2020. doi: 10.1016/j.carbpol.2020.116683.

[36] G. Lupidi, G. Pastore, E. Marcantoni, and S. Gabrielli, “Recent Developments in Chemical Derivatization of Microcrystalline Cellulose (MCC): Pre-Treatments, Functionalization, and Applications,” *Molecules*, vol. 28, no. 5. MDPI, Mar. 01, 2023. doi: 10.3390/molecules28052009.

[37] I. M. Aroso, A. R. Araújo, R. A. Pires, and R. L. Reis, “Cork: Current Technological Developments and Future Perspectives for this Natural, Renewable, and Sustainable Material,” *ACS Sustainable Chemistry and Engineering*, vol. 5, no. 12. American Chemical Society, pp. 11130–11146, Dec. 04, 2017. doi: 10.1021/acssuschemeng.7b00751.

[38] N. Gama, A. Ferreira, and A. Barros-Timmons, “3D printed cork/polyurethane composite foams,” *Mater Des*, vol. 179, Oct. 2019, doi: 10.1016/j.matdes.2019.107905.

[39] Q. Yang, H. Fukuzumi, T. Saito, A. Isogai, and L. Zhang, “Transparent cellulose films with high gas barrier properties fabricated from aqueous alkali/urea solutions,” *Biomacromolecules*, vol. 12, no. 7, pp. 2766–2771, 2011, doi: 10.1021/bm200766v.

[40] J. T. Carvalho, I. Cunha, J. Coelho, E. Fortunato, R. Martins, and L. Pereira, “Carbon-Yarn-Based Supercapacitors with in Situ Regenerated Cellulose Hydrogel for Sustainable Wearable Electronics,” *ACS Appl Energy Mater*, vol. 5, no. 10, pp. 11987–11996, Oct. 2022, doi: 10.1021/acsaem.2c01222.

[41] A. Abdisattar *et al.*, “Recent advances and challenges of current collectors for supercapacitors,” *Electrochem commun*, vol. 142, Sep. 2022, doi: 10.1016/j.elecom.2022.107373.

[42] S. L. Silvestre *et al.*, “Cork derived laser-induced graphene for sustainable green electronics,” *Flexible and Printed Electronics*, vol. 7, no. 3, Sep. 2022, doi: 10.1088/2058-8585/ac8e7b.

[43] T. Meng, Y. Xuan, and X. Zhang, “A Thermally Chargeable Hybrid Supercapacitor with High Power Density for Directly Converting Heat to Electricity,” *ACS Appl Energy Mater*, vol. 4, no. 6, pp. 6055–6061, 2021, doi: 10.1021/acsaem.1c00905.

[44] C. Chen, H. Qin, H. Cong and S. Yu, “A Highly Stretchable and Real-Time Healable Supercapacitor,” *Advanced materials*, vol. 31, 2019, doi 10.1002/adma.201900573.

[45] Y. Zheng, Z. Lin, W. Chen, B. Liang, H. Du, R. Yang, X. He, Z. Tang and X. Gui, “Flexible, sandwich-like CNTs/NiCo2O4 hybrid paper electrodes for all-solid-state supercapacitors,” *J Mater Chem A Mater*, v. 5, pp 5886-5894, 2017, doi:10.1039/C7TA00491E

[46] L. Li, E. B. Secor, K. S. Chen, J. Zhu, X. Liu, T.Z. Gao, J. W. T Seo, Y. Zhao and M. C. Hersam, “High-performance solid-state supercapacitors and microsupercapacitors derived from printable graphene inks,” *Adv Energy Mater*, v. 6, n. 20, Oct. 2016, doi:10.1002/aenm.201600909

[47] Y. G. Zhu, Y. Wang, Y. Shi, J. I. Wong, and H. Y. Yang, “CoO nanoflowers woven by CNT network for high energy density flexible micro-supercapacitor,” *Nano Energy*, n. 3, pp. 46-54, 2014 doi:10.1016/j.nanoen.2013.10.006

[48] D. Pech, M. Brunet, P-L.L. Taberna, P. Simon, N. Fabre, F. Mesnilgrente, V. Conédéra and H. Durou, “Elaboration of a microstructured inkjet-printed carbon electrochemical capacitor,” *J Power Sources*, v. 195, pp. 1266-1269, 2010, doi:10.1016/j.jpowsour.2009.08.085.

[49] J. Bin In, B. Hsia, J. H. Yoo, S. Hyun, C. Carraro, R. Maboudian, and C. P. Grigoropoulos, “Facile fabrication of flexible all solid-state micro-supercapacitor by direct laser writing of porous carbon in polymide,” *Carbon NY*, v. 83, pp. 144-151, 2015, doi: 10.1016/j.carbon.2014.11.017.

[50] Z. S. Wu, Z. Lui, K. Parvez, X. Feng, and K. Müllen, “Ultrathin printable graphene supercapacitors with AC line-filtering performance”, Adv Materials, n. 27, pp. 3669-3675, doi: 10.1002/adma.201501208.

[51] S. L. Kim, H. T. Lin and C. Yu, “Intercalated Graphene Oxide for Flexible and Practically Large Thermoelectric Voltage Generation and Simultaneous Energy Storage”, *Energy Materials*, v 48, pp. 582-589, June 2018, doi:10.1016/j.nanoen.2018.04.015

[52] A. Kundu and T. S. Fisher, “Harnessing the thermogalvanic effect of the ferro/ferricyanide redox couple in a thermally chargeable supercapacitor,” *Electrochim. Acta*, v. 281, pp. 357–369, 2018, doi: 10.1016/j.electacta.2018.05.164.

[53] X. Wu, B. Huang, Q. Wang and Y. Wang, “Thermally chargeable supercapacitor using a conjugated conducting polymer: Insight into the mechanism of charge-discharge cycle,” *Chem. Eng. J.*, v. 373, pp. 493–500, 2019, doi:10.1016/j.cej.2019.05.075.

[54] H. Cheng, X. He, Z. Fan and J. Ouyang, “Flexible Quasi-Solid State Ionogels with Remarkable Seebeck Coefficient and High Thermoelectric Properties,” *Adv. Energy Mater.*, v. 9, 2019, doi:10.1002/aenm.201901085.

[55] C.-G. Han, X. Qian, Q. Li, B. Deng, Y. Zhu, Z. Han, W. Zhang, W. Wang, S.-P. Feng, G. Chen and W. Liu, “Giant thermopower of ionic gelatin near room temperature,” *Science*, v. 368, pp. 1091–1098, 2020, doi:10.1126/science.aaz5045.

[56] S. L. Kim, J. Hsu and C. Yu, “Intercalated graphene oxide for flexible and practically large thermoelectric voltage generation and simultaneous energy storage,” *Nano Energy*, v. 48, pp. 582–589, 2018, doi:j.nanoen.2018.04.015

A

SUPPLEMENTARY FIGURES

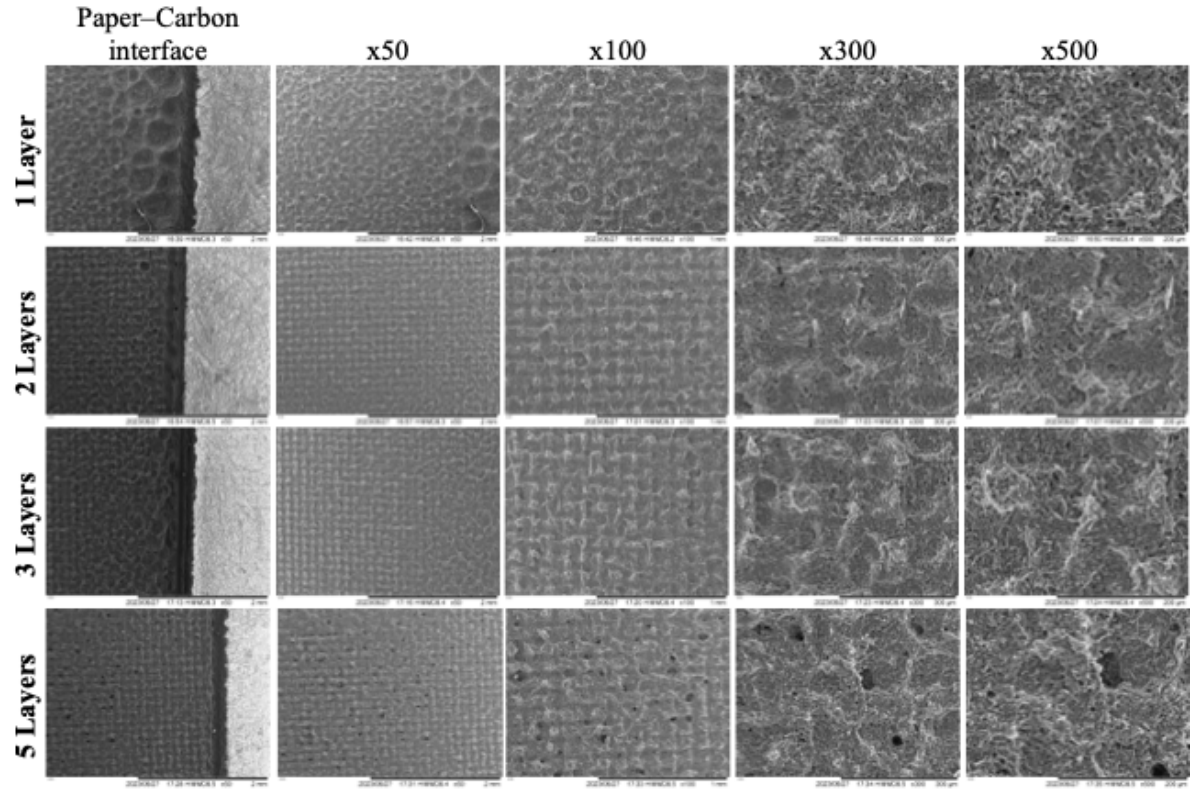

Figure 5.1 – shows a SEM images.

.

B

SUPPLEMENTARY TABLES

Table 5.1 – Examples of 2D planar SCs for printed electronics reported in literature.

SC architecture	Electrode materials	Substrate	Electrolyte	Capacitance	Energy Density	Power density	Capacitance retention (nr. of cycles)	Ref.
2D sandwich-type	Au NP/CNT/PAM/PPy (symmetric)	Free-standing	Au/PAM/ Na_2SO_4	885 mF cm^{-2} @1 mA cm^{-2}	123 μW h cm^{-2}	0.5 mW cm^{-2}	93 % (10 000) [b] 82 % (1000) [c]	[44]
	$NiCo_2O_4$ NS/CNT buckypaper (symmetric)	Free-standing	PVA/KOH	268.4 F g^{-1} @0.1 mA cm^{-2} 337.3 mF cm^{-2} @0.1 mA cm^{-2}	1.17 mW h cm^{-3}	2430 mW cm^{-3}	95.6 % (2000) [b]	[45]
	Graphene	Polymide	PVA/H_3PO_4	9.3 F cm^{-3} @0.25 A cm^{-3}	1.29 mWh cm−3	278 W cm^{-3}	>10,000 cycles	[46]
	CoO/CNT	PET	PVA/KOH	17.4 F cm^{-3}	3.48 mWhcm^{-3}	0.25 A cm^{-3}		[47]
	Activated carbon	SiO_2/Si	1 M Et_4NBF_4	2.1 mF cm^{-2} @1 mV s^{-}	—	—	—	[48]

2D inter-digitated finger-type	Porous carbon	Polymide	PVA/H_3PO_4	0.8 mF cm2 @10 mV s^{-1}	—	—	>3000 cycles	[49]
	Graphene/PEDOT	PET	PVA/H_2SO_4	348 mF cm^{-3} @1 V.s^{-1}	12 mWh.cm^{-3}	4386 W cm^{-3}	>50,000 cycles	[50]

Table 5.2 – Summary of TCSCs recently reported in literature.

Type of config-uration	Electrode	Substract	Electrolyte	Electrolyte ionic con-ductivity	Soret coefficient	Output thermally-in-duced voltage	Ref.
Sandwich-type	MWCNT-coated Au electrodes (thicker electrodes)	Glass	NaOH-treated PEO	8.13×10^{-5} S cm^{-1} (RT)	11.1 mV K^{-1}	180 mV (ΔT = 16 K)	[20]
	PANI-coated gra-phene/CNT	PTFE	PSSH	9 S m^{-1} (70% RH)	7.9 mV K^{-1} (70% RH)	38 mV (ΔT = 5.3 K)	[51]
	Carbon cloth	Free-standing	PVA/$K_3Fe(CN)_6$/ $K_4Fe(CN)_6$	5.44 mS cm^{-1} (RT)	0.86 mV K^{-1}	22.2 mV (ΔT = 30 K) 40.4 mV (ΔT = 50 K)	[52]
	PDAQ-BC/acety-lene black (weight ratio: 85 : 15)	Au-coated polyimide	PSSH	—	8.27 mV K^{-1} (ΔT = 5.2 K) 6.67 mV K^{-1} (ΔT = 10.8 K)	43 mV (ΔT = 5.2 K) 72 mV (ΔT = 10.8 K)	[53]
	SWCNT coated over Au	Glass	EMIM:DCA/PVDF-HFP (80wt. % EMIM:DCA)	6.7 mS cm^{-1} (RT, 67-75% RH)	26.1 mV K^{-1}	—	[54]
Planar-type	rSGO	PET film at-tached to a DVD disk	SGO	0.4 S m^{-1} (70% RH)	~5.7 mV K^{-1} (70% RH)	58 mV (ΔT = 10.5 K, 70% RH)	[55]
	TCSC module with 50 rSGO/SGO pairs	PET	SGO	—	4.53 mV K^{-1} (50% RH)	~20 mV (ΔT = ~4 K, ~50% RH)	[56]
	MWCNT	PET	PVA/H_3PO_4 (50wt. %)	7.85×10^{-5} mS cm^{-1} (50 wt. % H_3PO_4) 0.082 mS cm^{-1} (75 wt. % H_3PO_4)	2.35 mV K^{-1}	45 mV (ΔT = 20 K)	[18]

Table 5.3 – Resume of the electrochemical characterization of the cellulose electrolytes. The values show the average and the respective standard error of the mean obtained from three samples each.

Nomenclature	Thickness [mm]	$C_{f=10mHz}$ [μS cm^{-2}]	R_b [Ω]	σ_i [mS cm^{-1}]
CM0	0.182 ± 0.043	12.201 ± 4.193	24.25 ± 8.32	0.49 ± 0.28
GCM	0.233 ± 0.029	–	58.01 ± 28.21	0.27 ± 0.13
ECM	0.225 ± 0.017	15.505 ± 0.578	9.40 ± 1.47	1.37 ± 0.15

Table 5.4 – Resume of the electrochemical characterization of the developed CCEs by method 1. The values show the average and the respective standard error of the mean obtained from three samples each.

Nomenclature	Thickness [cm]	$C_{f=10mHz}$ [μS cm^{-2}]	R_b [Ω]	σ_i [mS cm^{-1}]
M1C2T5	0.303 ± 0.024	0.004 ± 0.002	1366.7 ± 71.8	0.012 ± 0.001
M1C2T15	0.411 ± 0.085	0.007 ± 0.001	1288.7 ± 67.0	0.018 ± 0.003
M1C2T30	0.493 ± 0.067	0.003 ± 0.001	1349.3 ±44.6	0.020 ± 0.003
M1C2T60	0.489 ± 0.025	2.223 ± 3.847	1141.0 ± 155.3	0.024 ± 0.005
M5C2T5	0.498 ± 0.030	11.484 ± 2.025	77.2 ± 31.5	0.352 ± 0.14
M5C2T15	0.367 ± 0.041	7.186 ± 0.863	24.4 ± 21.0	1.280 ± 1.01
M5C2T30	0.369 ± 0.052	5.758 ± 0.129	105.8 ± 9.2	0.199 ± 0.05
M5C2T60	0.423 ± 0.088	6.826 ± 1.770	53.2 ± 21.6	0.469 ± 0.10
M1C5T5	0.532 ± 0.093	14.786 ± 1.397	15.2 ± 4.1	2.03 ± 0.39
M1C5T15	0.569 ± 0.015	15.021 ± 1.628	13.7 ± 5.8	2.61 ± 0.92
M1C5T30	0.526 ± 0.058	16.018 ± 0.478	9.5 ± 3.7	3.37 ± 0.93
M1C5T60	0.547 ± 0.010	18.933 ± 1.974	10.7 ± 0.8	2.90 ± 0.18
M5C5T5	0.470 ± 0.063	0.879 ± 1.501	1164.0 ± 70.6	0.023 ± 0.004
M5C5T15	0.590 ± 0.057	3.595 ± 6.213	863.1 ± 648.6	0.103 ± 0.037

M5C5T30	0.660 ± 0.059	13.895 ± 0.754	383.3 ± 187.5	0.109 ± 0.037
M5C5T60	0.718 ± 0.042	4.281 ± 7.405	823.1 ± 641.3	0.128 ± 0.229

Table 5.5 – Resume of the electrochemical characterization of the developed CCEs by method 2. The values show the average and the respective standard error of the mean obtained from three samples each.

Nomenclature	Thickness [cm]	$C_{f=100mHz}$ [μS cm^{-2}]	R_b [Ω]	σ_i [mS cm^{-1}]
C2M100	0.719 ± 0.127	0.015 ± 0.010	1948 ± 940.5	0.023 ± 0.007
C2M50	0.587 ± 0.189	7.451 ± 10.527	1095.3 ± 165.1	0.030 ± 0.010
C5M100	0.727 ± 0.006	0.018 ± 0.010	1298 ± 104.7	0.032 ± 0.002
C5M50	0.666 ± 0.081	0.010 ± 0.004	1230.3 ± 205.1	0.031 ± 0.007

Table 5.6 – Resume of the electrochemical characterization of all TCSCs devices.

TCSCs	Specific Capacitance		Specific Power [c] (mW cm^{-2})	Specific Energy [c] (μW h cm^{-2})	ESR (1kHz) (Ω)
	@ 5mV s^{-1} (mF cm^{-2})[a]	@ 10μA cm^{-1} (mF cm^{-2})[b]			
TE1	1.33	1.87	0.181	0.165	538.3
TE2	1.61	2.11	0.206	0.186	726.9
TE3	1.80	3.08	0.176	0.272	439
BE1	1.77	2.35	0.195	0.207	684.6
BE2	1.52	2.28	0.474	0.201	829.9
BE3	1.78	2.58	0.195	0.227	688.3
BEC1	2.21	2.34	0.193	0.207	645.3
BEC2	2.63	3.38	0.329	0.298	573.1
BEC3	2.10	2.71	0.189	0.239	642.8

[a] CV measurement. [b] GCD measurement. [c] best value obtained.